Lab on a Chip

Accepted Manuscript

ROYAL SOCIETY OF CHEMISTRY

www.rsc.org/loc

ARTICLE TYPE www. rsc.org/xxxxxx | XXXXXXXX

Mass Transfer in the Biomolecular Binding of a Target Against Probe Molecules on the Surface of Microbeads Sequestered in Wells in a Microfluidic Cell†

Thomas F. Leary[a], **Setareh Manafi**[a] **and Charles Maldarelli***[a]

Received Xth XXXXXXXXXX 20XX, Accepted Xth XXXXXXXXX 20XX
First published on the web Xth XXXXXXXXXX 200X
DOI: 10.1039/b000000x

Diagnostic tools which screen the binding interactions of a protein target against a display of biomolecular probes to identify molecules which bind the target are central to cell proteomic studies, and to diagnostic assays. Here, we study a microfluidic design for screening interactions in which the probe molecules are hosted on microbeads sequestered in wells arranged at the bottom of a microfluidic flow channel. Assays are undertaken by streaming an analyte solution with a fluorescently labelled target through the cell, and identifying the fluorescing beads. Numerical simulations are first constructed for the analyte flow over the microbeads in the well array, and the increase in the target concentration on the microbead surface. The binding profile is expressed as a function of the ratio of the convective to the diffusive transport rates (Peclet number or *Pe*), and the ratio of the kinetic to the diffusive rates (Damkohler number, *Da*). For any *Pe*, as *Da* becomes small enough, the transport is determined by the intrinsic kinetic binding rate. As *Pe* increases, a thin concentration boundary layer develops over the top surface of the microbead because of the convective flow, and target binds more rapidly. However, the relatively stagnant layers of liquid in the well provide a diffusion barrier which slows the target transport, and for any *Da* and *Pe* the transport is slower than equivalent patches of probes arranged on the channel wall. Experiments are also undertaken at high *Pe*, using the binding of fluorescently labelled NeutrAvidin as a target to probes of its binding partner, biotin, on the microbead surface. The binding profile is compared to the simulations to measure the kinetic rate constant, and this comparison shows that the transport in the cell is not kinetically limited because of the diffusion barriers created by the stagnant liquid layer in the well. Simulations and experiments on microbeads which are only partially recessed in the well demonstrate an increase in the mass transfer rate as more of the microbead surface intersects the flow and the diffusion limitation due to the stagnant layer of liquid surrounding the bottom part of the microbead is minimized.

Introduction

Proteins direct biological processes by binding to other proteins or small biomolecules[1,2], for example enzymes bind to substrates, antibodies to antigens and ligands to receptors. Because of the importance of protein binding, tools which can screen, in a parallel and high-throughput format, the binding interactions of a target protein against a library of probe (or capture) molecules to identify binding pairs or quantitate the target find many applications[3], in fundamental studies of the cell proteome, in pharmaceutical drug, antibody and enzyme discovery[4–6], in the clinical diagnostic identification of disease markers and in biosensing for environmental surveillance and food monitoring[7,8]. The principal tools of parallel, high-throughput screening are the flat microarray (a miniaturization of the microtiter plate format) and the flow cytometric/microbead based assay (suspension arrays). In the microarray platform (reviewed in[9–22]) probes (i.e. proteins, antigens and antibodies, peptides, carbohydrates) are first robotically dispensed and bound as circular spots (typically a few hundred μm in diameter) on a substrate to form an array. The array, as a probe library, is subsequently incubated with an analyte solution containing potential binding partners (targets). After washing the chip to remove unbound target, binding is detected, usually by fluorescently labelling the target, and scanning for fluorescence at the spot locations with optical microscopy in a widefield mode. Flow cytometric/microbead based screens (for reviews see[21,23–30]) functionalize beads (typically 10-100 μm in diameter) to display probe molecules on their surfaces, and label the beads with a bar code (for example a luminecent spectral label) to identify the surface probe. Sets of microbeads, each with a common probe and label, are incubated with a fluorescently labelled analyte, and then passed single file through an excitation/detection op-

† Electronic Supplementary Information (ESI) available: See DOI: 10.1039/b000000x/

[a] *Levich Institute and Department of Chemical Engineering, The City College of the City University of New York, New York, New York 10031, USA. Fax: 212 650 6835; Tel: 212 650 8160; E-mail: charles@chemail.engr.ccny.cuny.edu*

tical beam in a flow cytometer to discriminate binding events and read the barcode. Although each are parallel and high-throughput venues which offer as well the multiplexed ability to screen several targets, they have their advantages and drawbacks. The spotted microarrays require less analyte and reagents than the flow cytometric/microbead assays because of their miniaturized design, and the robotic spotting facilitates the compilation of a probe library registry without the encoding which is required of the micro bead platform. In addition, with spotted microarrays, binding can be continuously monitored making them convenient for kinetic studies, while flow cytometric assays obtain signals at only a single time, making them inconvenient for kinetic studies. However, the binding surfaces in the microbead assays are the surfaces of suspended particles rather than the flat spots of the microarrays, and as such have the advantage of a larger probe surface binding area per analyte interrogation volume[31] which enhances the assay sensitivity. The microbead format also has the advantage in that the transport of target to the probe surface during the incubation step is faster relative to the microarray platform because the convective mixing streams target directly over the bead surface, and therefore incubation times can be shorter in comparison to microarrays which rely on diffusive transport through stagnant layers to bring the target to the surface.[32,33]

The diffusion barriers to mass transfer in flat microarrays can be reduced by incorporating the flat probe array as the inside surface of a microfluidic flow channel, and streaming the analyte through the channel, intersecting microfluidics with screening assays . This fluidic arrangement has been used to display a single probe along a relatively large channel area, or multiple probes in smaller, spotted areas, in the development of optical microfluidic biosensors[34–37]. Multiple probes have also been displayed on the flat walls of a microfluidic channel by lining the inside surfaces of parallel channels of a flow cell with probes (each channel with a separate probe), and streaming a target analyte through all the channels[38–41].

In this study we examine a microfluidics platform for screening in which microbeads displaying surface probes are assembled as an array into fixed positions on the bottom surface of a microfluidic flow cell and target analyte is streamed over the probe-bound beads for binding, a format which incorporates advantages of both the flat microarray and the flow cytometric/microbead array for parallel, high-throughput screening.[42–45] In general, several methods exist to pattern immobilized microbeads on a flat substrate surface. Microbeads can be deposited by gravity from a solution placed above the surface, and then affixed to the surface by using electrostatic interactions[46–50], covalent bonding[51,52], or an adhesive layer[53], or by transferring a pre-formed arrays of beads onto an adherent surface[54,55].

However, capturing beads by gravity-settling in an array of wells inscribed on a surface (a well-plate) presents a simpler solution since it does not rely on bead/surface interactions, and, by properly sizing the wells to be only slightly larger than the microbead diameter, single microbeads can captured at the array (well) location, which simplifies the tracking and correlation of screening events. Walt and collaborators[56] first pioneered the trapping of beads with surface probes in wells for screening applications by etching wells into the tips of individual fibers of a fiber optic bundle to form a well-plate, an approach which also allowed for individual readouts of fluorescently labeled binding events. Incorporating a well-plate filled with beads into a microfluidic cell can be undertaken in either of two ways. As studied by McDevitt et al[57–68] and Bau et al[69–71], beads are first trapped in the wells of a well-plate, and the plate is then incorporated as the bottom of a microfluidic flow cell.

Instead of ex-situ assembly, microbeads can also be assembled directly into an array in a microfluidic cell in one step by using an unfilled well-plate as the cell bottom, and streaming a suspension of beads through the cell to allow them to settle into the wells (see Fig. 1 and refs.[72,73] who also demonstrated the use of the array for a binding assay). To enhance the capture in this format, electric and magnetic fields have been applied to charged or paramagnetic beads (respectively) to direct the beads into the wells[74–76]. Fluid suction has also been used to assist in the bead capture; holes placed at the bottom of the wells provide a liquid path from the channel above the wells to drains and applying suction though these holes drives the beads into the wells (Ketterson[77]) and also enhances fluid flow around the beads and mass transfer of analyte during the screening step (see McDevitt et al.[57–68])

Here we use the microfluidic/microbead array platform in which the bead array is assembled by gravity in situ in the device (Fig. 1), and focus on the mass transfer in the binding of the target to the probes on the bead surface. Studies of target-probe mass transfer in microfluidic displays of probes have centered primarily on the analysis in the standard biosensor

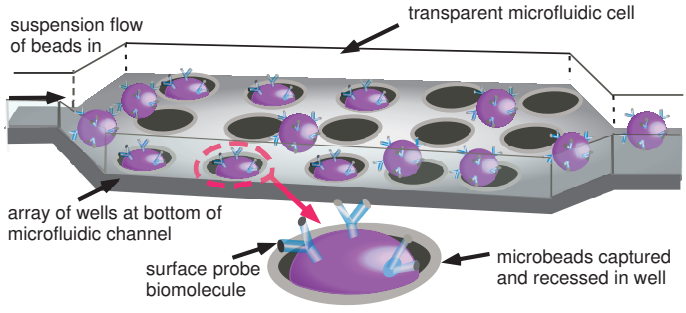

Fig. 1 Idealized schematic of the assembly of a microbead array by the gravitational settling of microbeads into wells incorporated as the bottom of a broad channel of rectangular cross section in a microfluidic cell.

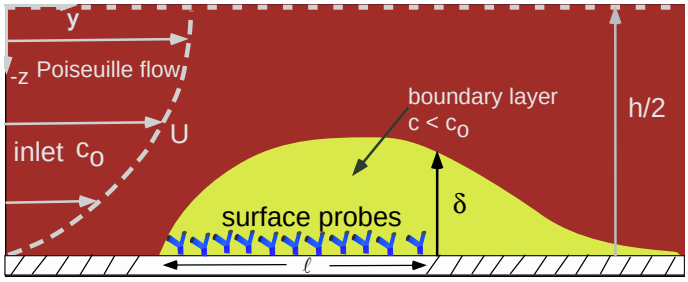

Fig. 2 The development of a boundary layer (yellow) for the mass transfer of a target to a surface patch of probes on the bottom wall of a microchannel.

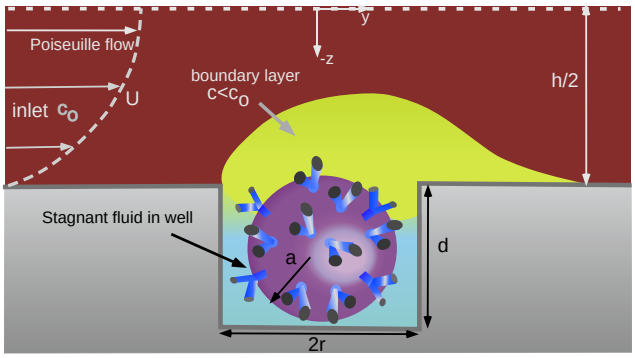

Fig. 3 The development of a boundary layer (yellow) over a microbead situated completely in a well on the bottom wall of a microchannel. The relatively stagnant liquid in the well is only replenished of target by diffusion, and its concentration becomes rapidly depleted (shading blue, a lower concentration than in boundary layer) due to the surface binding.

geometry of a surface patch of capture probes localized on the bottom surface of a microfluidic channel[78–99]. In this case, as shown in Fig. 2, the analyte solution of target molecules flows over the patch, and target kinetically binds to the probes on the surface. The kinetic binding lowers the concentration of target at the surface. As a result, a diffusion gradient of target develops across the flow streamlines which brings target from the bulk at high concentration to the surface at low concentration. When the timescale for the flow across the surface is much faster than the diffusion time of target to the surface (the usual condition in microfluidic assays as we describe later on), this diffusion concentration gradient is localized in a thin boundary layer at the surface, with the concentration of target approximately equal to the inlet concentration outside of the layer (Fig. 2). The binding rate is determined by the in-series processes of diffusion to the surface through the boundary layer, and kinetic bindng to the surface. The higher the flow, the thinner is the boundary layer and the greater is the diffusive flux to the surface. These leads to larger binding rates until the binding rate is only determined by the surface kinetics. This kinetic control represents the limiting condition for which the binding rate is the largest. The transport rates of target to surface patches of probes under diffusion and kinetic limitations have been the subject of several studies[78–99], and we review this literature in the following section.

The mass transfer of target to surface receptors on microbeads situated in wells arrayed at the bottom of a flow channel presents a more complex target mass transfer than the transport to a patch of receptors on a channel surface, and transport in this microbead geometry has not been studied in the detail of the surface patch geometry. As shown in Fig. 3, target streams over the top part of the microbead surface exposed to the flow, and at very large convective rates of target relative to diffusion, a boundary layer develops at the top of the microbeads which enhances the mass transfer. Along the bottom part of the microbead, the streaming flow is cut-off by the well and target has to diffuse through a relatively stagnant region of fluid to reach the bottom part. Thus the primary difference between the surface patch and the microbead sequestered in well geometries is that the boundary layer contacts the entire probe surface area when the probes are arranged as patches on a planar surface, while only contacts part of this area when the probes are on microbeads situated in wells. Thus we can expect the mass transfer to be hindered in the case of probes on microbeads in wells relative to probes on planar patches for similar probe surface areas. The few studies of the mass transfer of a target convectively flowed over a microbead array of surface probes in a microfluidic flow channel have been undertaken by Bau et al[71,100] and McDevitt et al[101,102]. Bau et al[71] studied the geometry of microbeads sandwiched between the top surface of the flow channel and a shallow well at the bottom of the channel, obtaining solutions for the target concentration on the microbead surface as a function of the surface kinetics and the flow (Peclet number). The surface concentration as a function of time compared favorably to experiments undertaken on the binding of quantum dot labelled biotin as a target to NeutrAvidin surface probes. In the Bau[71] geometry, the surface of the microbeads is readily accessible to the flow since the microbeads are fixed by sandwiching between the top and bottom walls of the channel. McDevitt et al first began to examine the implications of well confinement on target-probe binding, and simulated the transport of target over microbeads situated in a pyramidal-shaped well, with flow through the well bottom channeled by a hole underneath the microbead. These simulations demonstrated how the drain flow enhance the target mass transfer, and the model reproduced experiments presented on the binding of a labelled antigen as a target to antibody surface probes.

Our focus is on microbeads situated in wells without a drain (Fig. 3), which is a less complicated microfluidic microbead array screening platform, but a geometry which more strongly confines the flow and mass transfer. Our objective is to first compute, by numerical simulation, the surface con-

centration of the target on the microbead surface for varying conditions of flow rate, and rates of diffusion and kinetic binding, and in particular to assess the effects of the attenuated flow by comparing, under identical conditions, the transport of target to probe functionalized microbeads in microchannel wells to the transport to a probe-display of patches on the microchannel wall. Second, target-probe binding experiments are undertaken on a microbead array assembled by capture in a well plate, using the binding of a fluorescently labelled protein NeutrAvidin, as a target, to its binding partner, biotin, displayed on the microbead surface. The experiments display only the single probe (biotin), and screen against one target (NeutrAvidin), although the format can be extended to a library of different probes of biologicals (e.g. antibodies) screening a number of targets (e.g. antigens). The aim of the experiments is to illustrate how the simulations can be used to measure the surface kinetic binding rate constant, and to demonstrate that, because of the well confinement, the mass transfer of target is a mixed convective diffusion and kinetic binding process, and both elements of the transport need to be incorporated to obtain the correct kinetic rate constant. We consider in detail the case in which the microbead is completely sequestered in the well (Fig. 3) with well depths approximately equal to the microbead diameter. However, we will also study the configuration in which the microbeads are positioned in wells of smaller depth than the microbead radius so that a larger surface area of the microbead intersects the flow in which the well depths are only half the diameter of the microbeads, so that a greater area of the functionalized surface of the microbeads intersects the flow, and the boundary layer extends further around the microbead surface so the mass transfer is improved. This represents a simple solution to the attenuation of the mass transfer for microbeads completely sequestered in the wells, and we demonstrate both theoretically and experimentally that the mass transfer is indeed improved.

Review of Transport Theory for Microfluidic Binding of Target To Probes on a Planar Surface

As shown in Fig. 2, a rectangular surface patch of capture probes (length ℓ and width t_s) is localized in a rectangular channel of width w and height h with $t_s \approx w$ and $h \ll w$ so that the mass transport is primarily two dimensional. Target analyte enters the flow cell with concentration c_o and streams over the patch in Poiseuille flow $\mathrm{v}_y(z) = \frac{3U}{2}\left\{1-4\left\{\frac{z}{h}\right\}^2\right\}$, where U is the average velocity, and y and z are along and perpendicular to the flow, respectively. The transport of the target molecule in solution to the channel wall is a mixed in-series process consisting of diffusion across the (parallel) convective flow streamlines, and kinetic binding of the target to the probe once the target has arrived to the sublayer of solution immediately adjoining the surface[95]. The time scale for a target molecule to be convected along the patch is $t_c = \ell/U$, and the time scale for the target to diffuse across the channel is $t_{\mathcal{D}} = h^2/\mathcal{D}$ where $\mathcal{D}$ is the target diffusion coefficient. The ratio of these scales, $t_c/t_{\mathcal{D}} = \frac{\ell/h}{Pe}$ defines a Peclet number ($Pe = Uh/\mathcal{D}$). Typically, $h \sim 10^2\mu$m, $w \sim 10^3\mu$m and $U \sim 10-10^4\mu$m/s corresponding to flow rates $Q \sim 10^{-1}-10^2$ $\mu\ell$/min. Target proteins or smaller biomolecular ligands have molecular weights of order 10^3-10^4 and corresponding diffusion coefficients of $\sim 10^2\mu$m^2/s so that the Pe is large, of order $10-10^4$. If the sensor patch ℓ is short enough such that $\ell/h < Pe$, then the time for diffusion across the channel is longer than the time required for the target to move over the patch ($t_c < t_{\mathcal{D}}$), and target can only reach the surface through a boundary layer with a thickness, which increases with distance down the channel but is always smaller than h. The target concentration outside of the boundary layer is approximately equal to the inlet concentration c_o (Fig. 2). The thickness of the boundary layer at the end of the patch, which we denote as δ, is determined, for a given Pe by the ratio of the patch length ℓ to the height h. This thickness can be estimated as the thickness for which the time for diffusion across this thickness to the patch is equal to the time for a target molecule riding at a distance δ from the wall to reach the end of the patch[95]. Typically $\ell > h$, and two regimes usually apply in the parameter space of Pe. In the first, when the Pe number is not very large (i.e. $Pe > 1$) and $\ell/h < Pe$ the boundary layer thickness at the end of the patch is sizable relative to h since $\frac{\delta^2}{\mathcal{D}} \sim \frac{\ell}{U}$ or $\frac{\delta}{h} \sim \left\{\frac{\ell/h}{Pe}\right\}^{1/2}$. (Here we have characterized the velocity in the boundary layer as scaling with U.) In the second regime, $Pe \gg 1$ and $\ell/h \ll Pe$, and the boundary layer thickness relative to h becomes asymptotically small in Pe everywhere along the patch. In this case, the flow in the boundary layer is approximately linear in the direction normal to the surface ($\mathrm{v}_y \approx 6(U/h)(h/2-|z|)$). The boundary layer thickness at the downstream end of the patch, scales as $\frac{\delta^2}{\mathcal{D}} \sim \frac{\ell}{\{U/h\}\,\delta}$ or $\frac{\delta}{h} \sim \left\{\frac{\ell/h}{Pe}\right\}^{1/3}$.

At the patch surface the diffusive flux is equal to the kinetic rate (per unit area) with which target binds to the surface probes. A general framework for describing the kinetic binding of a solute molecule (of area $\mathcal{A}_t$ projected on the surface) to binding sites (of area $\mathcal{A}_p$ and density Γ_p) on a surface can be formulated in terms of a generalized Langmuir equa-

tion[103–106]

$$\frac{\partial}{\partial t}\left\{\frac{\Gamma}{\Gamma_\infty}\right\} = k_a c_s \phi - k_d \left\{\frac{\Gamma}{\Gamma_\infty}\right\} \quad (1)$$

where Γ is the surface concentration of target, Γ_∞ is the maximum concentration of target which can bind, t is time, c_s is the sublayer concentration of target at the surface and k_a and k_d are the association and disassociation rate constants, respectively and ϕ is the fraction of sites available when the target concentration is Γ. When the surface density of probes (Γ_p) is small enough such that bound target does not overlap $\Gamma_p \mathcal{A}_t < 1$, the maximum concentration of bound target is equal to the probe density $\Gamma_\infty = \Gamma_p$ and the fraction of sites available is $\phi = 1 - \frac{\Gamma}{\Gamma_p}$, leading to the Langmuir kinetic scheme. Under many circumstances, the target's projected area is much larger than the probe area, and surface densities can be large enough so that $\Gamma_p \mathcal{A}_t \geq 1$. In this case, as binding proceeds, binding of targets becomes sterically hindered, and the fraction of sites available is not given by $\phi = 1 - \frac{\Gamma}{\Gamma_p}$. Models for ϕ to account for steric hindrance based on Monte Carlo simulations of random sequential adsorption (RSA) have been developed (e.g.[105]). An approximate method is to assume that $\phi = 1 - \frac{\Gamma}{\Gamma_\infty}$ where the maximum packing is given from the RSA model for $\Gamma_p \mathcal{A}_t >> 1$ as $\Gamma_\infty = 0.556/\mathcal{A}_t$, in which case the binding is also Langmuirian. Hence in this study we will adopt the Langmuir kinetic scheme. In this scheme, the equilibrium surface density (Γ_{eq}) is $\frac{\Gamma_{eq}}{\Gamma_\infty} = \frac{k}{1+k}$ where $k = \frac{k_a c_o}{k_d}$. During the binding process, the sublayer concentration initially decreases due to kinetic binding, but at later times increases as the surface begins to saturate, causing the kinetic flux to decrease and the diffusive flux to repopulate the sublayer.

For $Pe \gg 1$ and $\ell/h \ll Pe$, the diffusive flux to the surface through the boundary layer scales as $\frac{\mathcal{D}\{c_o - c_s\}}{\delta}$, where c_s is the sublayer concentration. The maximum kinetic flux of target to the surface, as is clear from eq. 1, is obtained in the early times of binding when there is little target bound ($\phi \to 1$). Equating this maximum kinetic flux ($k_a \Gamma_\infty c_s$) to the diffusive rate defines a scale for the sublayer concentration, $\frac{c_s}{c_o} \sim \frac{1}{1 + Da\left\{\frac{\ell/h}{Pe}\right\}^{1/3}}$, where the Damkohler number Da is defined as $Da = \frac{k_a \Gamma_\infty h}{\mathcal{D}}$. In the limit $Pe \gg 1$ and $\ell/h \ll Pe$, when $Da\left\{\frac{\ell/h}{Pe}\right\}^{1/3} \gg 1$ (fast binding kinetics relative to diffusion), the sublayer concentration tends to zero. This mass transfer controlled regime has been studied extensively as the entrance region problem[78,93], with analytical expressions for Γ as a function of t and the distance along the sensor surface. When, for $Pe \gg 1$ and $\ell/h \ll Pe$, $Da\left\{\frac{\ell/h}{Pe}\right\}^{1/3} \ll 1$ the binding kinetics are slow relative to diffusion, and the sublayer concentration remains at the inlet concentration. (This is also true for arbitrary Pe and ℓ/h if $Da \to 0$.) The process is only controlled by the binding kinetics, and $\frac{\Gamma(\tau)}{\Gamma_{eq}} = 1 - e^{-\varepsilon Da(1+\frac{1}{k})\tau}$ where $\varepsilon = \frac{c_o h}{\Gamma_\infty}$ (see Goldstein et al who have extended this analytical solution for small Da[85,86]). For intermediate values of Da and $Pe > 1$, analytical solutions can be obtained for $\Gamma/\Gamma_{eq} \ll 1$[93,98]. When the surface concentration is not negligible, analytical solutions cannot be obtained because of the nonlinearity of the kinetic equation. For $Pe \gg 1$ and $\ell/h \ll Pe$ and Da of order one, boundary layer (two compartment) models in which the Langmuir kinetic equation and a relation equating the boundary layer flux to the net kinetic adsorption are integrated either numerically in time for the average surface concentration on the patch[79–84,87–89] or analytically[99]. These two compartment models equate the diffusive flux of target to the surface (formulated in terms of a boundary layer mass transfer coefficient k_L) to the kinetic rate of binding of the target to the surface, i.e. $k_L\{c_o - c_s\} = k_a c_s\{\Gamma_\infty - \Gamma\}$ where we have assumed a Langmuir formulation, although other more complex models have been used. The bulk mass transfer coefficient k_L can be used as a fitting parameter to data, or can be specified approximately from the asymptotic analysis assuming the sublayer concentration equal to zero (i.e. $\frac{hk_L}{\mathcal{D}} = 1.28 Pe^{1/3}\left\{\frac{h}{\ell}\right\}^{1/3}$[99,107]). Over the past several years, numerical solutions by finite element or finite difference solution of the convective diffusion equation for the target coupled to the kinetic exchange at the patch boundary have been obtained for arbitrary values of Pe, Da and ℓ/h to obtain the surface concentration of target as a function of time and distance along the patch[90–99], and these have been compared with the two compartment model solution and the results of binding experiments (see for example[40,108]). These studies have shown that the two compartment models yield accurate results for a wide range of values of k_a as long as the Peclet number is large enough (several hundred or more), and the adsorption depth, Γ_∞/c_o, is large relative to h ($\varepsilon \ll 1$) so that bulk diffusion gradients scale with the boundary layer thickness and not the adsorption depth (cf. in particular Hansen et al.[99]).

Transport Simulations of Target-Probe Binding to a Microbead in a Well

For the simulations, we consider the mass transfer of target to probes on the surface of a microbead situated in an isolated, circular well located at the bottom of a microfluidic flow channel of rectangular cross section. The values for the geo-

metric parameters are set to be equivalent to the experimental design, the channel height h = 80 μm, the well depth d = 50 μm and diameter $2r$ = 70 μm as in Fig. 3. (Simulations in which the microbeads are only partially recessed are detailed with the comparison to the corresponding experiments in the Experimental Section, further on.) The microbead with diameter a = 42.3 μm is positioned along the axis of the well, and is recessed, as in the experiments. The microbead is located equidistantly ($\pm$ 4 μm) from the top and bottom of the well. In the experiments, the microbeads rest at the bottom of the wells; the offset of 4 μm allows a more simplified mesh construction for the finite element simulations which decreased the calculation time. A separate set of flow and mass transfer simulations were undertaken for decreasing separation distances between the microbead and the well wall, and these differed by only a few percent in the average surface concentration on the microbead surface relative to the 4 μm offset simulations. The isolated well is positioned centrally with respect to the side walls of the channel, with the well axis a distance $w/2$ from the walls set so that the sidewalls do not affect the results. The computational domain is closed by entrance (upstream) and exit (downstream) cross sections of the channel located a distance L from the well center chosen so that the entrance and exit also do not affect the results.

In the experimental platform, wells are not isolated but arranged in a pattern of rows (perpendicular to the flow), with rows separated by 250 μm, and with the wells in each row separated by 250 μm. The wells in each row are offset from the next by 125 μm so the downstream distance between wells directly behind each other is s = 500 μm. The simulations reproducing the experiments are for Pe = O(10^3). The diffusion boundary layers around the microbeads in the wells positioned downstream from each other act as if they are isolated if the concentration across the boundary layer becomes uniform (due to diffusion normal to the channel wall) in the convective time required for the fluid to travel between the wells. For large Pe, assuming the boundary layer thickness δ at the downstream end of the well is of order $\dfrac{\delta}{h} \sim \left\{\dfrac{2r/h}{Pe}\right\}^{1/3}$ (as given by the expression for surface patches with the patch length $\ell \sim 2r$), and the fluid velocity in the boundary layer is of order $U\delta/h$, the ratio of the transit time between wells $sh/(U\delta)$ to the diffusion time $\delta^2/\mathcal{D}$ is $s/(2r) \sim 10$. Therefore the boundary layers between the wells tend to relax, and the simulation of an isolated well approximates accurately the mass transfer in the experiments presented in this study.

The flow of the analyte stream provides the convective flow setting for the mass transfer of the target, and is described first. The analyte is modeled as an incompressible, Newtonian fluid with the density ρ and viscosity μ of water at 20°C (ρ=10^3 kg m^{-3} and μ = 10^{-3} kg m^{-1}sec^{-1}) independent of the analyte concentration. The flow through the channel is driven by a pressure gradient, and is implemented by assigning a uniform velocity U in the flow direction across the inlet, and a zero pressure (relative to the inlet) across the exit. The flow is assumed to be steady, and is governed by the continuity (mass conservation) and Navier-Stokes equations [107],

$$\nabla \cdot \tilde{\mathbf{v}} = 0 \tag{2}$$

$$\mathfrak{R}\left[\tilde{\mathbf{v}} \cdot \nabla \tilde{\mathbf{v}}\right] = -\nabla \tilde{p} + \nabla^2 \tilde{\mathbf{v}} \tag{3}$$

where the nondimensional variables ∇ and ∇^2 are the gradient and Laplacian operators (scaled by h), $\tilde{\mathbf{v}}$ is the velocity vector (scaled by U), $\tilde{p}$ is pressure (nondimensionalized by $\mu U/h$), and $\mathfrak{R} = \dfrac{\rho U h}{\mu}$ is the Reynolds number. For the experimental flow conditions, typical for microfluidic screening, $U \approx 10$ - 10^4 μm sec^{-1}, the flow Reynolds number is of order 10^{-3}- 1, and therefore the flow is primarily dominated by viscous forces retaining limited inertial effects. The continuity and Navier-Stokes equations are solved in cartesian coordinates (x, y, z as shown in Fig. 3) with the inlet and outlet conditions, and boundary conditions of no slip on the interior walls of the channel and well and the bead surface. The solution is obtained numerically using finite elements, implemented with the COMSOL Multiphysics simulation package, 4.2, with the basic fluid CFD module, for the flow solution, and the chemical reacting engineering module for the mass transport simulations. The FEM calculations used both triangular and quadrilateral meshes. In the absence of the well, and when L is sufficiently large, the (steady) flow at the origin is a unidirectional Poiseuille flow through a rectangular cross section (height h and width w), independent of y and given by [109]

$$\begin{aligned} \mathrm{v}_y(z,x) =& \frac{3U\chi}{2}\left(1 - \left[\frac{z}{h/2}\right]^2\right) \\ & -6U\chi \sum_{n=0}^{\infty} \frac{(-1)^n}{\lambda_n^3 \cosh\left(\lambda_n w/h\right)} \cos\left(\frac{\lambda_n z}{h/2}\right) \cosh\left(\frac{\lambda_n x}{h/2}\right) \end{aligned} \tag{4}$$

where $\chi^{-1} = \left[1 - 6\left(\dfrac{h}{w}\right)\sum_{n=0}^{\infty} \lambda_n^{-5} \tanh\left(\dfrac{\lambda_n w}{h}\right)\right]$ and $\lambda_n = \dfrac{(2n+1)\pi}{2}$. A distance $L = 3\times10^3 \mu$m is found to be large enough so that this Poiseuille flow is obtained when with sufficient mesh density for w/h = O(1), and this provides a first validation of the flow simulations. w is then taken much larger than h ($w = 3\times10^3 \mu$m) so that the Poiseuille flow becomes independent of x (at the well), and the side walls do not influence the flow at the well. These flow simulations (and the resulting mass transfer simulations) are therefore in the absence of hydrodynamic effects associated with the channel inlet, outlet or side walls.

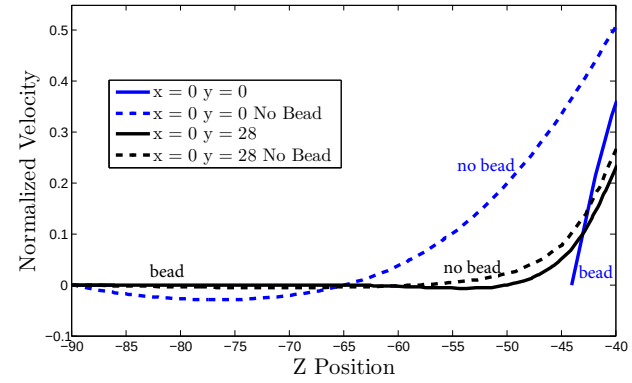

(a)

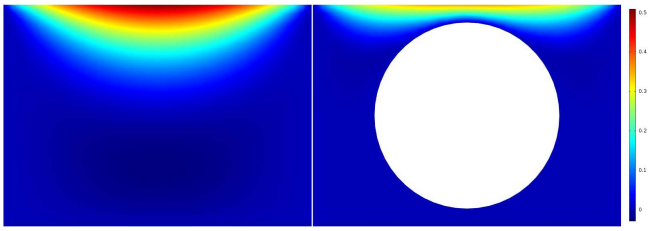

(b)

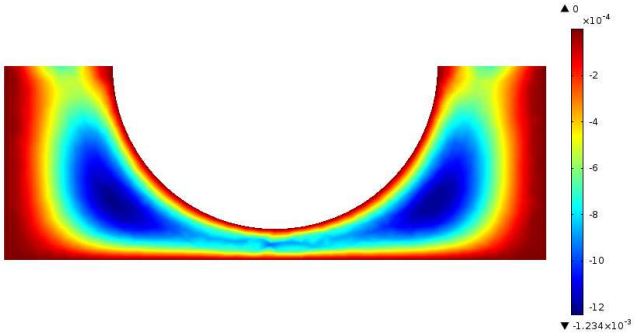

(c)

Fig. 4 (a) Velocity in the y direction (normalized by the average velocity U) as a function of z, in the plane $x = 0$, at the center of the well ($y = 0$) and at an upstream location inside the well and between the bead and the well wall ($y = 28$ μm) in the presence and absence of a microbead. (b) Magnitude of the velocity in the plane $x = 0$ inside the well in the absence and presence of a microbead. (c) The y component of the velocity in the plane $x = 0$ for the bottom half of the microbead in the well. All simulations are for $\Re$=1.

When the well is unoccupied, the hydrodynamics is an open cavity flow[110], as shown for $\Re = 1$, in Fig. 4(a) for the y component of the velocity profile (normalized by the average velocity U) as a function of z for $x = 0$ and $y = 0$ (the well centerline), and $x = 0$ and $y = 28$ μm corresponding to a location inside the well and in the upstream direction. (In the plane $x = 0$, the well wall is at $y = \pm 35$ μm, $z <$ -40 μm.) Fig. 4(b) (left) is a plot of the magnitude of the velocity field in the plane $x = 0$. In this plane, in the absence of the bead, a separatrix streamline dips into the well a distance z of $\approx$ 10 μm (20 percent of the well depth) on the well centerline, and separates recirculating flow in the cavity from the primarily unidirectional flow in the y direction in the channel (note the change in sign of the y component of velocity). The recirculation consists of one large eddy, as would be expected since the aspect ratio of the well $d/(2r) = 5/7$ is less than one, and consecutive, oppositely rotating eddies at the center develop for deep, rather than shallow wells[110]. The y component of the velocity on the well axis, which is, for z = -40 μm approximately one half of the average velocity, decreases exponentially with distance $-z$ into the well. The flow pattern in the presence of the microbead, also for $\Re$=1, is also shown in Figs. 4(b) (right). The separatrix streamline in the x =0 plane is forced upwards by the bead, and a circulation develops between the microbead and the well wall, although, as evidenced by the magnitude of the y component of velocity at the off axis position (y = 28 μm, Fig. 4(a)) is very small below the separatrix. The y component of the normalized velocity in the x = 0 plane for the bottom half of the microbead in Fig. 4(c) shows the return part of the circulation as negative values of the y-component of the velocity. As is clear from the scale bar in Fig. 4(c), the circulation velocity is of order of 10^{-4} - 10^{-4} of the average velocity U. Additional information on this circulation, including the vorticity map, is provided in the electronic supplementary information (*ESI*). These flow patterns make apparent that when the well is occupied by a bead, the direct streamline flow in the channel only contacts directly the microbead surface at the top of the microbead where the separatrix streamline dips down to the microbead surface, and the remainder of the microbead surface is contacted by a very slow circulating flow which separates from the mainstream.

Simulations of the rate at which targets bind to the probes on the surface of the microbeads in the wells from the analyte solution streaming over the beads is obtained by solving the convective-diffusion equation (eq. 5) for the mass conservation of the target (in cartesian coordinates) using a finite element numerical simulation with forward marching in time and also implemented with COMSOL.

$$\frac{\partial \tilde{c}}{\partial \tau} + Pe\, \tilde{\mathbf{v}} \cdot \nabla \tilde{c} = \nabla^2 \tilde{c} \qquad (5)$$

In the above, $\tilde{c}$ is the concentration of target (nondimensionalized by the inlet concentration c_o), $\tilde{\mathbf{v}}$ is the steady velocity obtained above, and, as in the Introduction, $Pe = Uh/\mathcal{D}$ and time is scaled by the diffusion time $t_{\mathcal{D}} = h^2/\mathcal{D}$. We assume at the inlet cross section that the concentration of target is uniform (c_o), and the distribution has relaxed completely at the exit so that the derivative with respect to the flow direction y is equal to zero. Eq. 5 is solved with these conditions, and assuming zero flux of solute on the interior channel and well surfaces, and equating the diffusive flux to the kinetic binding at the microbead surface.

$$\{\mathbf{n}\cdot\nabla\tilde{c}\}_{\text{bead}} = Da\left[\tilde{c}_s\left\{1-\left[\frac{k}{1+k}\right]\tilde{\Gamma}\right\}-\frac{\tilde{\Gamma}}{1+k}\right] \quad (6)$$

$$\frac{\partial\tilde{\Gamma}}{\partial\tau} = \varepsilon\left[\frac{k}{1+k}\right]\{\mathbf{n}\cdot\nabla\tilde{c}\}_{\text{bead}} \quad (7)$$

where $\mathbf{n}$ is the outward normal to the microbead surface, $\tilde{c}_s$ is the nondimensional sublayer concentration and, as before, $\varepsilon = \dfrac{c_o h}{\Gamma_\infty}$ (Γ_∞ is the maximum surface concentration of target), $Da = \dfrac{k_a\Gamma_\infty h}{\mathcal{D}}$ and $\tilde{\Gamma}$ is the surface concentration scaled by the equilibrium concentration, Γ_{eq}, where $\dfrac{\Gamma_{eq}}{\Gamma_\infty} = \dfrac{k}{1+k}$ and $k = \dfrac{k_a c_o}{k_d}$ (k_a and k_d are the adsorption and desorption rate constants). The surface concentration is a function of the position on the bead surface, and we denote by $\bar{\Gamma}$ the average value on the bead surface. The mesh and time step are refined until $\bar{\Gamma}(\tau)$ is independent of the mesh density and the time step.

In nondimensional form, the target binding $\bar{\Gamma}(\tau)/\Gamma_\infty$ is a function of the Damkohler and Peclet numbers, k and ε. In the experiments to be described later on the binding of NeutrAvidin to surface biotin, the binding equilibria is nearly irreversible ($k \gg 1$), and therefore, to be in congruence with the experiments, we undertake simulations for infinite k. The parameter ε scales the overall time for equilibration. In most screening applications the concentration of the target is low enough or the binding capacity large enough so that the adsorption depth, Γ_∞/c_o - the distance above the surface containing enough material to saturate the surface per unit area - is large relative to the channel height h so that $\varepsilon \ll 1$. This is also true in the experiments, and we set $\varepsilon = 0.015$ in the simulations which is the experimental value. We first examine the case of Pe = 10, a value at the low end of the range of values of the Peclet number in microfludic screening. In Fig. 5(a) is given the surface concentration of targets as a function of time ($\bar{\Gamma}(\tau)$) for Da = 1, 10 and 10^2 for binding to the surface of a microbead in a well. This binding rate on the microbead surface is compared to the binding of target from a Poiseuille flow onto a circular patch of probes situated centrally at the bottom of the microchannel wall ($z = -h/2$), and

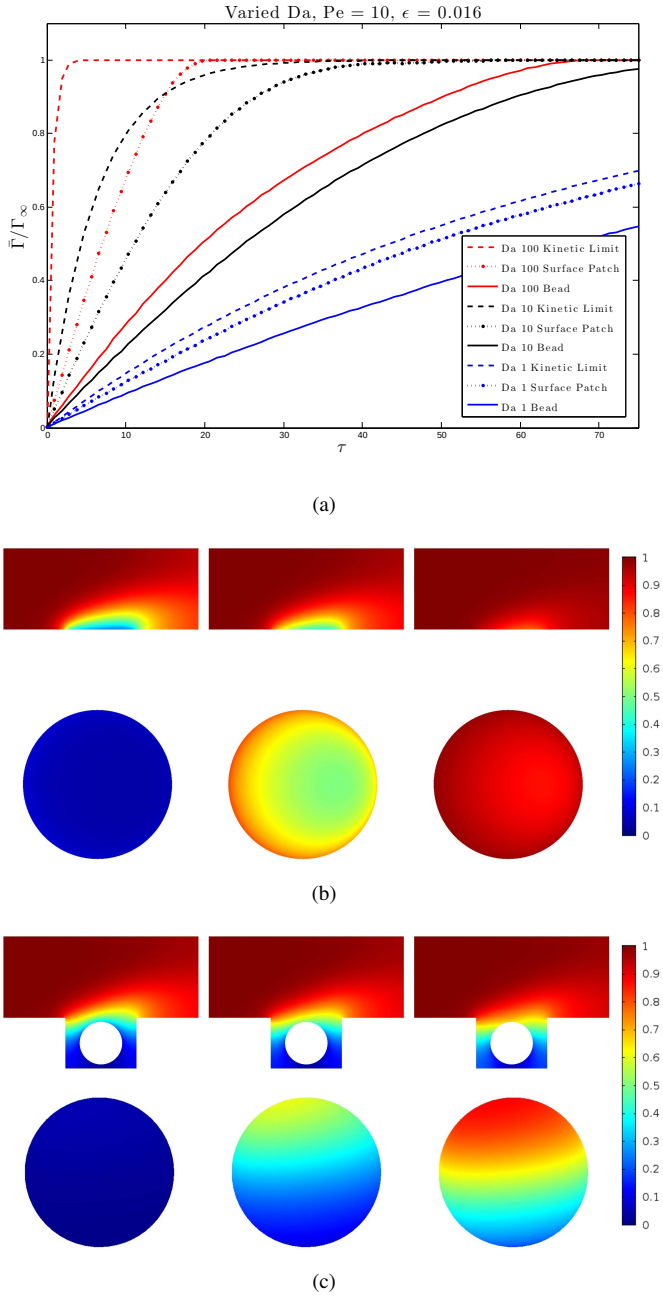

Fig. 5 Target binding to probes on a circular patch on a microchannel wall and on the surface of a microbead in the well for Pe = 10: (a) The average nondimensional surface concentration on a surface patch and the surface of the microbead, $\bar{\Gamma}$, as a function of τ for Da =10, 10^2 and 10^3. (b) Side view in the plane $x = 0$ of the target concentration boundary layer above a circular patch, and the spatial distribution of bound target on the patch as a top view (z=-40 μm). (c), Side view, in the plane $x = 0$, of the boundary layer around a microbead in the well, and side view of the surface concentration on the microbead surface as a projection on the circle of the concentration on the hemisphere $x > 0$. In b) and (c), the snapshots are for τ = 1, 15 and 30 and Da = 10. The simulations are for ε = .016 and $k \to \infty$.

with a radius equal to the well radius r and with the binding capacity Γ_∞ and kinetic rate k_a identical to that on the microbead surface. In the nondimensional form presented in Fig. 5(a) with τ nondimensionalized by the diffusion time scale, increasing Da corresponds to a binding experiment in which the kinetic binding rate k_a is increased, with the average velocity U, concentration c_o, binding capactity Γ_∞ and diffusion coefficient $\mathcal{D}$ held fixed. For both the circular patch and the microbead surface, the concentration of bound target increases monotonically with τ, and as *Da* increases, the binding rate is observed to increase. The binding of target to the surface probes is a transport process of bulk diffusion to the surface followed by the kinetic step of target-probe conjugation. The process begins as target in the sublayer of analyte immediately adjacent to the probe surface binds to the surface, depleting the sublayer concentration $\tilde{c}_s$. Depletion continues until the surface kinetic rate becomes reduced by the partial saturation of the surface, in which case bulk diffusion repopulates the sublayer until the sublayer returns to c_o (nondimensionally to one). For the smallest values of *Da*, kinetic exchange is much slower than bulk diffusion, and the sublayer concentration remains relatively uniform around the microbead or above the patch, eliminating diffusion barriers. In this limit, the average surface concentration is given by the exponential expression $\bar{\Gamma}(\tau)/\Gamma_\infty = 1 - e^{-\varepsilon Da \tau}$. This ideal kinetic limit represents the fastest rate at which target can bind to the surface, and this limiting envelope is shown in Fig. 5(a). For *Pe* = 10, this kinetic limit is only coincident with the numerical simulations for the patch and the microbeads for $Da \leq 0.1$ (data not shown). As *Da* increases to values of one and larger, the kinetic rate increases relative to diffusion and this reduces the concentration of target in the sublayer of analyte immediately adjacent to the surface, c_s, to values less than c_o, creating a diffusive barrier to binding. Since the sublayer concentration is no longer equal to the farfield bulk concentration, but is smaller, the numerically simulated mixed diffusive-kinetic binding rate falls below the ideal kinetic limit, as is evident for *Da* =1, 10 and 10^2 in Fig. 5(a). For increasing *Da*, the sublayer concentration decreases and this has two consequences: First the numerically simulated mixed binding rate increases as the diffusive flux to the surface is greater the lower the sublayer concentration. Second, relative to the ideal kinetic limit, the mixed simulated binding becomes increasingly slower (Fig. 5(a)) since the kinetic limit assumes the sublayer concentration is equal to the farfield concentration.

Fig. 5(a) also makes clear that, because target binds more quickly to the patch interface than to the microbead surface for a given *Da*, the diffusive barrier which develops around the microbread is much larger than the diffusive barrier which develops over the patch. The reason why the diffusive flux to the surface of the microbead is smaller than to the surface of the patch is because the diffusive transport in the case of a patch is entirely through a convective boundary layer, while for the microbead is through a convective boundary layer over the top of the bead exposed to the flow, but through a trapped, slowly recirculating flow which surrounds the bottom part of the bead. The bulk concentration fields and the surface concentrations provide more detail and insight into this difference in mass transfer between the two geometries. Consider first binding to the circular patch of probes; the concentration above the patch in the plane x = 0 (perpendicular to the microchannel wall, along the flow and at the center of the patch), and the surface concentration in the plane z = -40 μm (the channel wall) for *Da* = 10 and for three nondimensional times, is shown in Figs. 5(b). For this relatively small value of *Pe* (10), the characteristic patch size in the flow direction ($\ell \sim 2r$), relative to the channel cross section h ($2r/h = 7/8$), is still less than *Pe*, and as discussed in the Introduction for binding to a patch, for $\ell/h < Pe$, a boundary layer forms over the patch and extends into the streaming flow but does not extend to the opposite end of the channel, as is clear in Figs. 5(b). The concentration in the boundary layer above the patch shows the initial depletion in the concentration next to the surface due to the large value of *Da*, followed by an increase in the sublayer concentration as the surface begins to saturate. As the boundary layer is thinner at the upstream part of the patch, the diffusive flux is greater at the front end of the patch, and the surface concentration increases and saturates from the upstream to the downstream end of the patch, Figs. 5(b).

For the binding of the target to the microbead surface, the concentration field in the plane $x = 0$ and the surface concentration along the hemisphere $x > 0$ (projected onto a circle) for *Da* = 10 and for same three times as depicted for the patch, are shown in Fig. 5(c). Again, the characteristic length of the probe area in the streamwise direction $\ell \sim 2a$ divided by h ($\ell/h = 1/2$) is smaller than *Pe*, and a boundary layer forms above the separatrix. In the region in which the separatrix is directly attached to the microbead surface, target diffuses unobstructed through the convective boundary layer to the surface, and the diffusive flux is the largest and the binding rate to the surface the greatest. This resembles the transport to the surface of the patch. At the upstream and downstream parts of the well where the separatrix dips into the well, target diffuses through the convective boundary layer and then through the slowly recirculating liquid surrounding the lower half of the microbead in the well to reach the bead surface. The diffusion through the essentially stagnant liquid reduces the diffusive flux, and the liquid in the well quickly becomes depleted of target for this relatively large value of *Da*. As a result, while the binding rate at the top part of the microbead surface increases rapidly, the surface concentration along the lower part increases much more slowly (cf. the projection of the surface concentration), providing an overall reduction in the average rate of binding ($\bar{\Gamma}(\tau)$) compared to the rate of binding

for a patch. The depletion of target in the stagnant liquid in the well is slowly replenished, and the equilibration takes a much longer time relative to either the patch equilibration or the ideal kinetic limit. As with the patch geometry, the binding to the surface is asymmetric with respect to the flow direction. The top part of the microbead, in contact with the thinner part of the boundary layer and having the larger diffusive flux, has a greater rate of binding relative to the downstream part of the microbead, in contact with the thicker part of the boundary layer and a reduced diffusive flux. As Da decreases and the ideal kinetic limit is approached, the effect of the stagnant layer around the microbead in the well in decreasing the diffusive flux is reduced, and the microbead and patch geometries show similar binding rates. For $Da \leq .1$ (data not shown), the concentration of target in the stagnant layer is approximately the farfield target concentration due to the large kinetic barrier (relative to diffusion), and the binding rate becomes identical to the kinetic limit.

When the Pe number is increased to a value of 10^4 (Fig. 6), the transport picture changes significantly for both the patch and microbead geometries. As discussed in the Introduction, when, for large Pe, the characteristic streamwise length of the probe area, ℓ, divided by the channel height h is much smaller than Pe, convective boundary layers of target over the probe surface develop and become very thin. The corresponding diffusive flux of target through the layer becomes much larger relative to order one Pe, and this increases the binding rate of the target to the probe surface. In addition, because of the enhanced diffusion rate, for any value of Da (and particularly large values), the sublayer concentration of target adjoining the probe surface is not depleted by kinetic adsorption to the extent that it is when $Pe = O(1)$, and the mixed diffusive-kinetic binding becomes closer to the ideal kinetic limit. These results are evident in Fig. 6(a) for $\bar{\Gamma}(\tau)$ which shows clearly that, for $Pe = 10^4$, the binding rates for both the patch and the microbead geometries ($\ell/h \ll Pe$) are much faster than for $Pe = 10$ (compare Figs. 5(a) and 6(a)) at the same values of Da, and are closer to the ideal kinetic limit, and Figs. 6(b) - 6(c) where the boundary layers are much thinner and depletion less evident when compared with $Pe = 10$ and Da = 10 (compare Figs. 5(b) - 5(c)). Consider in particular first the patch geometry. For Da = 1, the mixed diffusive-kinetic binding rate is on the kinetic envelope. This is in agreement with the criteria established in the Introduction, for which kinetically limited transport is valid for streamwise patch lengths ℓ satisfying $\ell/h \ll Pe$ when $Da\left\{\frac{\ell/h}{Pe}\right\}^{1/3} \ll 1$ (for Da = 1, $Da\left\{\frac{\ell/h}{Pe}\right\}^{1/3} \approx 0.1$). For the larger values of Da in Fig. 5(a), $Da\left\{\frac{\ell/h}{Pe}\right\}^{1/3} \geq 1$, the kinetically limited criteria is not satis-

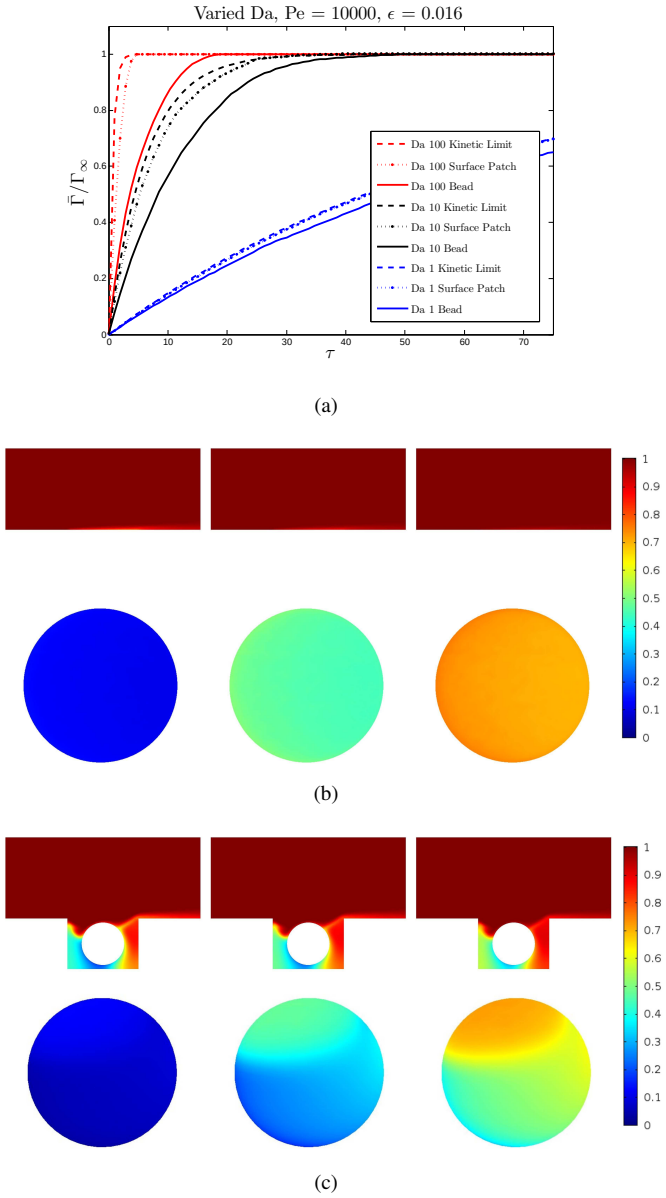

Fig. 6 Target binding to probes on a circular patch on a microchannel wall and on the surface of a microbead in the well for $Pe = 10^4$: (a) The average nondimensional surface concentration on a surface patch and the surface of the microbead, $\bar{\Gamma}$, as a function of τ for Da =10, 10^2 and 10^3. (b) Side view in the plane $x = 0$ of the target concentration boundary layer above a circular patch, and the spatial distribution of bound target on the patch as a top view (z=-40 μm). (c), Side view, in the plane $x = 0$, of the boundary layer around a microbead in the well, and side view of the surface concentration on the microbead surface as a projection on the circle of the concentration on the hemisphere $x > 0$. In b) and (c), the snapshots are for τ = 1, 15 and 30 and Da = 10. The simulations are for ε = .016 and $k \to \infty$.

fied, and as is evident in the figure, the mixed diffusive-kinetic patch simulations are below the ideal kinetic limit. In the case of binding to the microbead surface, some depletion of target still occurs in the stagnant liquid surrounding the lower part of the microbead, due to the slower diffusive transport in this liquid. The liquid inside the well at the upstream side appears to be more depleted of target compared to the liquid at the opposite side, and correspondingly the binding rate is slower on the lower part of the upstream end of the microbead surface relative to the bottom part of the downstream end. This contrasts with the case of Pe = 10 (Figs. 5(c)) in which depletion and binding were more symmetrical. One reason for this asymmetry may be due to the fact that the boundary layer along the separatrix at the upstream side of the well is very thin due to the high Pe and follows the contour of the separatrix streamline which dips into and out of tthe well just upstream of the microbead. As a result, a strong (lateral, y directed) diffusive flux is directed to the microbead surface along the ascending part of the streamline (i.e. the part that moves out of the well and just next to the target-binding bead surface) reducing the z directed flux through the separatrix required to bring target to the lower part of the microbead on the upstream side. When the Peclet number is small and equal to 10, the boundary layer is much thicker and extends well above the separatrix at the upstream side (Figs. 5(c)) and lateral diffusion is not as significant and transport is principally in the downward z direction. In any case, the reduced diffusive flux through the stagnant layer surrounding the microbead in the well accounts for a large barrier, and kinetically limited transport is only observed for Da of approximately 0.5.

Experimental Measurements of Target-Probe Binding Rate Constants Using the Microfluidic Microbead Array

This section illustrates experimentally how the simulations of the binding of target to probes in the microfluidic microbead array screening platform can be used to accurately measure the target-probe binding kinetic constants, and demonstrates how the simulations can be used to optimize for the binding rate. We choose the well known binding of an avidin protein (NeutrAvidin, MW 60000) (as a target) to its ligand binding partner, the small molecule vitamin (H) biotin (MW 244) (as a probe displayed on the microbead surface). NeutrAvidin is a commercially synthesized protein. As with its natural analogues Avidin and Steptavidin, NeutrAvidin is homotetrameric, with four binding sites for biotin. Two sites are located on one face of the protein molecule, and two are on the opposite face. The sites bind with high selectivity and affinity (in solution, K = 10^{15} M for Avidin and NeutrAvidin, and 10^{13} M for Streptavidin)[111–113]. NeutrAvidin is a deglycosylated form of Avidin with a pI of 6.3, which makes it slightly negatively charged at neutral pH. The design and fabrication of the microfluidic cell with a well plate as the bottom surface of a wide channel in the cell is described first, followed by the procedure for the functionalization of the microbeads with biotin and finally the method for assembling the array and screening with the target NeutrAvidin. Fluorescently labelled NeutrAvidin is streamed over the microbeads and allowed to bind to the biotin on the microbead surface to equilibrium. From measurements of the increase in fluorescence intensity on the bead surface relative to the equilibrium value, experimental curves of the surface concentration of target (relative to the equilibrium surface concentration) are constructed as a function of time and compared to simulations to infer the kinetic constants.

Microfluidic Cell and Microbead Functionalization

The microfluidic geometry consists of a wide central channel with lateral dimensions of 15 x 5 mm and a height of 100 μm. The bottom wall of the channel is a flat surface populated by a uniform array of circular wells 70 μm in diameter and either 50 μm deep (for completely recessed microbeads) or 25 μm for partially recessed microbeads. The lateral pitch of the array is 250 μm and sequential rows are offset by 125 μm. The channel is connected to four ports. Entrance and exit ports are located at opposite ends of the channel to control microbead deposition rates, remove excess microbeads from the surface, and introduce analyte solution using syringe pumps. Two ports located on the sides of the channel are used to introduce different sets of microbeads, although only one set is used in these experiments. The cell is fabricated in two layers, which are subsequently bonded, a bottom layer which consists of the well plate, and a top layer, consisting of the wide central channel, channels to connect the entrance, exit and bead introduction ports to the central duct, and circular entryways at the ends of the connecting channels for tube insertions. The two halves are made using soft lithography, by molding the prepolymer polydimethylsiloxane (PDMS) on masters fabricated in a negative topology by photolithographic patterning of an epoxy polymer resist spun to a prescribed thickness on a silicon wafer. Holes are punched in the top layer (from the opposite side on which the channels are molded and into the circular entryways) and after binding the two halves, a glass support slide is bound to the lower layer and polyethylene tubing is inserted in the holes. After sealing and glass slide mounting, the inside surfaces of the flow cell are functionalized using silane chemistry with an oligomeric polyethylene glycol (PEG) layer to minimize nonspecific adsorption of the target protein to the channel surfaces, and to provide a cushion over which the microbeads can move during entrapment[114]. The experimental protocol is described in detail in the supplementary information.

The microbeads used in the experiments are soda-lime glass calibration microbeads with a mean diameter of 42.3 μm (Thermo Fisher Scientific, Inc.; $\pm$ 1.5 μm standard deviation in the size distribution). They were selected for ease of functionalization and sized so that only a single bead could occupy each well. Glass beads have the additional advantage of a large density difference with water to facilitate gravity-based capture in the wells of the array. The surface of the beads are functionalized with the biotin probe by using an aminosilane to functionalize the glass microbeads with primary amine groups, and subsequently using a N-hydroxysuccinimide ester derivative of biotin (NHS-Biotin) to link biotin to the surface amines by the formation of an amide bond between the ester and the amine. These details are described in the electronic supplementary information (ESI).

Measurement of NeutrAvidin-Biotin Binding Kinetics

To measure the NeutrAvidin-Biotin binding kinetics, one set of microbeads, displaying biotin as a probe molecule, are arrayed in the wells of the microfluidic channel. To introduce the functionalized beads into the microfluidic channel, the device is submerged in deionized water under a vacuum to remove air bubbles. Polyethylene tubing is inserted into the access ports, and the tubing connecting to the entrance port is attached to a plastic syringe controlled by a syringe pump (Harvard Apparatus, PHD). The bead sets are suspended in water by magnetic stirring and drawn into 250 and 500 $\mu\ell$ glass syringes. The glass syringe is then connected to the loading port on the side of the microchannel, elevated above the device and positioned with the needle facing down so that the beads fall out of the needle, into the tubing and down towards the microchannel under gravity. Fluid flow in the channel is initiated at 10 $\mu\ell$/min so that the beads entering the channel are immediately propelled along the surface of the well array and begin depositing into the wells. Beads that are not captured by the wells accumulate in the exit port and are not carried into the exit tubing because of the moderate flow rate. They are returned to the channel by reversing the flow direction using the syringe pump so that the beads are directed towards the entrance port. The flow direction is switched repeatedly until the desired well occupancy is achieved. The flow rate is then increased to 500 $\mu\ell$/min (in the forward direction), resulting in the propulsion of the beads out of the exit port and into the exit tubing.

After the microbeads have been sequestered in the wells, the tubing connected to the inlet port is removed and replaced by tubing connected to a glass syringe containing the target protein solution, NeutrAvidin. The protein is fluorescently tagged with Texas Red (NeutrAvidin-Texas Red, Pierce) and is diluted from a stock solution (1 mg/$m\ell$ to a concentration of c_o = 250 ng/$m\ell$ (4.2×10^{-9} M) to be used as the target analyte in the microfluidic cell. All protein solutions are prepared in phosphate buffered saline (PBS, pH 7.4, Fisher). The stock solution was filtered to remove unbound fluorescent labels by using a dye removal resin column (Pierce), and stored at 4^{o}C; the target analyte solution is prepared immediately before the experiment at room temperature. NeutrAvidin-Texas Red is streamed over the assembled array at a flow rate of 100 $\mu\ell$/min corresponding to an average velocity U through the channel of 3.3×10^3 μm/sec. The diffusion coefficient of the avidin protein has been measured by Spinke et al.[115] and is equal to 6.0×10^{-11} m^2/sec which results in a value for *Pe* of 5600. The microbead fluorescence is observed under a NikonEclipse TIE inverted microscope with an LED light source, a 10x/NA=0.3 (air) objective in epifluorescence mode, and recorded using a filter cube for the Texas Red fluorescence (excitation 560$\pm$ 40 nm and emission 630 $\pm$ 75 nm) and a Nikon DigiSight camera. A motorized stage for scanning different areas of the array is used to reconstruct a stitched image of the array containing approximately 50 wells. Given in Fig. 7 are images of the microbead fluorescence in the assembled array as a function of nondimensional time (for comparison to the simulations). Time is scaled by $\tau_{\mathcal{D}} = h^2/\mathcal{D} = 166.7$ sec.) From this data, the cumulative fluorescence on each bead can be measured by summing the recorded fluorescence at each pixel location lying within a circular perimeter circumscribing the bead fluorescence. The fluorescence measurements are continued until equilibrium is reached on each bead as indicated by a constant cumulative fluorescence on the microbead. For each individual microbead, the cumulative at each time divided by the equilibrium cumulative fluorescence defines the normalized fluorescence which is equivalent to the average concentration of the target on the microbead surface divided by the equilibrium concentration ($\bar{\Gamma}/\Gamma_\infty$), assuming the surface concentration is linear in the fluorescence. At each time t, the individual normalized microbead fluorescence is measured on each of several tens of microbeads in the array (the reconstructed view of Fig. 7) and averaged, to obtain an average value for the normalized concentration$\bar{\Gamma}/\Gamma_\infty$ as a function of t. The averaged $\bar{\Gamma}/\Gamma_\infty$ is presented as a function of τ in Fig. 8 for the experiment shown in Fig. 7 as well as two other experiments, with error bars for each experimented obtained from the standard deviation of the individual microbead measurements at each time.

The experimental measurements of Fig. 8 can be simulated to calculate the Neutravidin-biotin kinetic rate constant k_a. The density of the biotin surface probes (Γ_p), as determined by the grafting density of the aminosilanes, is typically of the order of 0.2 - 0.4 molecules/ nm^2, or 250 - 500 $\AA^2$/site (see the discussion in the ESI), which is smaller than the binding face of the NeutrAvidin protein ($\mathcal{A}_t$) which as been measured by crystallography on the surface crystallized protein to be equal to 3025 $\AA^2$.[111]. Hence $\Gamma_p\mathcal{A}_t$ is in the approxi-

(a)

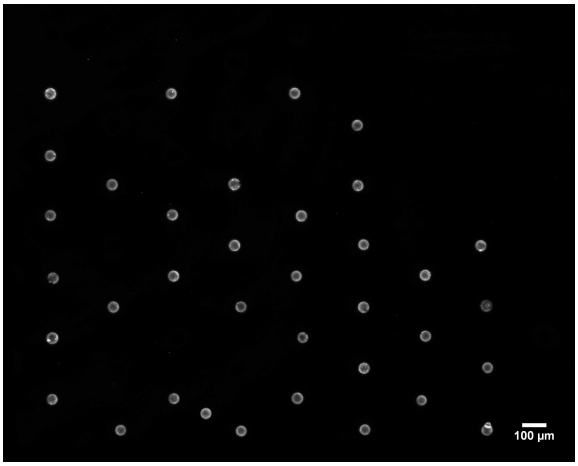

(b)

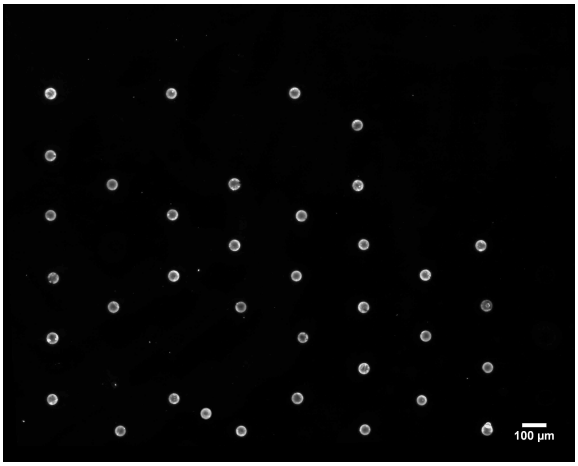

(c)

Fig. 7 Fluorescence images of the emission of Texas Red labelled NeutrAvidin bound to microbeads displaying surface biotin as a function of nondimensional time for c_o= 4.2×10^{-9} M. (a) τ = 9, (b) τ= 40, (c) τ = 135.

mate range of 6 to 12. Thus as the protein adsorbs it blocks unbound biotin sites, and in the general kinetic equation (eq. 1), the available site function ϕ cannot be set to $1-\Gamma/\Gamma_p$. As discussed earlier, one approximation, based on random sequential adsorption models, is to set ϕ equal to $1-\frac{\Gamma}{\Gamma_\infty}$, where Γ_∞ is the maximum packing density of the binding molecule, and is given for $\Gamma_p\mathcal{A}_t \gg 1$ by Γ_∞ = .556/$\mathcal{A}_t$ [105]. We use this approximation for the binding of NeutrAvidin to surface biotin and calculate $\Gamma_\infty = 2.75\times10^{-8}$ mole/m^2 for NeutrAvidin. We assume further that the binding is essentially irreversible, i.e. $k = k_a c_o/k_d \gg 1$, and verify this assumption (see below). We also note that after a NeutrAvidin molecule binds to the surface, a second biotin ligand can also bind because of the high density of the probes. However the cumulative fluorescence measures only the target binding, and cannot distinguish a ligand insertion into the second pocket. (A desorption study could show the effect of a second binding.)

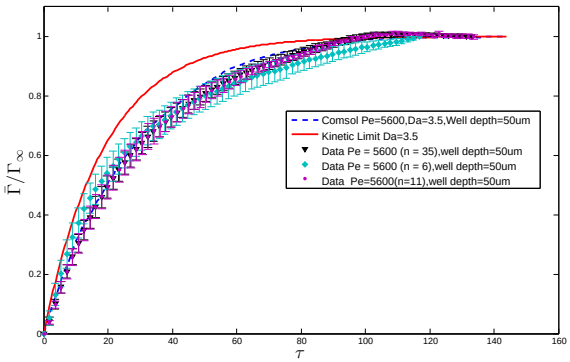

Fig. 8 Normalized binding curve $\bar{\Gamma}/\Gamma_\infty$ as a function of nondimensional time τ for well depth = 50 μm and comparison with simulation for Pe = 5600, Da = 3.5, ε = .015 for c_o = 4.2×10^{-9}M.

Using the irreversible (pseudo) Langmuir equation to describe the kinetic step, COMSOL mass transfer simulations are used to predict $\bar{\Gamma}/\Gamma_\infty$ as a function of k_a, and to compare to the experiments of Fig. 8. The conditions of the experiment correspond to Pe = 5600 and ε = .015 since h=100 μm, $\mathcal{D}$ = 6.0×10^{-11} m^2/sec, U = 3.3×10^3 μm/sec, Γ_∞ = .556/$\mathcal{A}_t$ and c_o=4.2×10^{-9} M, and hence the simulations are set to these values. An initial estimate of k_a is obtained by fitting the data to the irreversible pseudo Langmuir equation (assuming no diffusion barrier so $c_s = c_o$) using a least squares minimization procedure to minimize the global error of the sum of the square differences between the data and the exponential prediction of the kinetic equation at the times for which the data is recorded. This initial estimate of k_a is then increased in steps

(since the presence of a diffusion barrier decreases the effective value of k_a), and the COMSOL calculations are used to provide the simulation of $\bar{\Gamma}/\Gamma_\infty$ as a function of time for the incremented values of k_a. The global error is computed, and a minimum in the global error as a function of k_a is identified to establish the numerical value of the kinetic constant. We find $Da = 3.5$, and a value for $k_a = 7.63 \times 10^4$ $M^{-1}sec^{-1}$, and the simulation fit is shown alongside the experimental data in Fig. 8. Fig. 8 also shows the ideal kinetic limit for this value of Da and ε, and it is clear that the transport is not kinetically limited, with diffusion barriers exerting a strong effect.

We found that if the flow rate is increased by one order of magnitude, this higher flow rate dislodges microbeads from the wells, so experiments for Pe of order 10^5 were not undertaken. For smaller Pe, as in the range of 10-100, the slow convection creates depletion in the streaming fluid as the cumulative boundary layer thickness at the end of the cell, estimated as $\frac{\delta}{h} \sim \left\{ \frac{30 \times 2r/h}{Pe} \right\}^{1/2}$ where 30 is the number of wells in a single column extending downstream, is greater than 1/2 and the boundary layers reach the top wall of the channel. In this case, microbeads at the downstream end of the cell are not subject to a uniform concentration of target equal to c_o, and hence do not correspond to the single well conditions of the simulation. For Pe of order 10^3 - 10^4, the cumulative boundary layer thickness is only a fraction of h, and depletion is negligible, so the experiments were undertaken in that range.

With regard to the value we have obtained, other kinetic studies on the binding of Avidin proteins to surface biotin have been undertaken, primarily with biotin displayed on lipid bilayers, and all using a Langmuir kinetic scheme[116–119]. Conboy et al[119] used second harmonic generation (SHG) to measure the binding of Avidin to a surface supported biotinylated bilayer of the phospholipid DOPC with 4 mole percent biotinylated lipid with a spacer arm to extend the biotin from the bilayer to make it more accessible to the protein[119]. (The biotin displayed on the surface of the microbeads in our experiment was not extended by a spacer arm from the PEG layer.)The bilayer was assembled by vesicle fusion to the surface of a prism configured in a flow cell for the SHG measurement, and the composition of the vesicles were doped with 4 mole percent of a lipid with biotin linked to its head group, so that biotin can be displayed on the bilayer surface. Protein solutions at different bulk concentrations were injected into the cell and allowed to bind to the biotinylated surface. SHG measurements at the prism surface during the binding provided the surface concentration as a function of time (relative to the saturation value) which was fit to the Langmuir kinetic expression (assuming no diffusion gradients so $c_s = c_o$) to obtain values for k_a and k_d. They find $k_a/k_d = 1.6 \times 10^8$ M^{-1} and $k_a = 9.8 \times 10^3$ $M^{-1}sec^{-1}$. Reichert[116] measured the binding of fluorescently labeled Streptavidin to a Langmuir-Blodgett monolayer of archaic acid, deposited on the fiber optic tip of a biosensor by a Langmuir Blodgett technique. The archaic acid spreading solution for the Langmuir Blodgett deposition was doped with a biotinylated lipid (DHPE without and with a spacer arm), and the mole fraction of the biotinylated lipid in the monolayer was varied from 0 to 1. As with the bilayer studies of Conboy et al, the fiber tip was assembled into a flow cell, and protein solutions were injected into the cell and allowed to bind to the biotin in the monolayer on the fiber tip. Measurements of the protein fluorescence at the tip surface as the binding proceeds (recorded through the tip) allows the surface concentration of protein (relative to the saturation) to be obtained as a function of time as in our experiments, and these are then fit to the Langmuir kinetic model, again without considering bulk diffusion, to obtain the kinetic constant k_a. Measurements were also undertaken for desorption from a monolayer saturated with Streptavidin, by injecting a solution without protein into the flow cell after the monolayer had been equilibrated and again compared with Langmuir equation to obtain the desorption rate constant k_d. They find k_a/k_d of order 10^9 - 10^{11} M^{-1}, and k_a of order 10^4 $M^{-1}sec^{-1}$ - 10^5 $M^{-1}sec^{-1}$ for mole fractions of biotin in the monolayer varying from 0.1 - 1.0 (with and without spacer arms). Using the values for k_a/k_d from these articles as a guide, it is clear that for our experiment $k_d/(k_a c_o) \ll 1$, and the assumption that the binding is irreversible is validated.

To compare our values with these experiments, we note first that our study was undertaken under the condition that $\Gamma_p \mathcal{A}_t$ is in the approximate range of 6-12, where protein covers unbound biotin as it binds. Conboy et al's experiments are also in this regime of binding overlap, although the overlap is not as large: If we assume a lipid area per molecule of 60 $Å^2$, $\Gamma_p \mathcal{A}_t$ is approximately equal to 2 for a 4 mole percent doped monolayer, and therefore binding of the protein covers one additional biotin. In the archaic monolayer experiments, Reichert et al assume an area per molecule of the acid and lipid of 20 and 40 $Å^2$ per molecule, respectively, and calculate from these assumptions, values of $\Gamma_p \mathcal{A}_t$ for the mole fractions of the lipid in the monolayers they used in their experiments. Their measurements at mole fractions equal to 4.76 and 6.25 correspond to $\Gamma_p \mathcal{A}_t$ equal to 5.2 and 7.6, which approximate our estimated range, and they obtain values of k_a equal to 2.89 and 1.5×10^4 $M^{-1}sec^{-1}$ for these fractions, respectively, which, as the Conboy et al value, are smaller than our value. The difference, despite the fact that all are in the regime in which protein binding overlaps unbound biotin, can be attributed to two reasons. First, the different values may reflect the difference in the surfaces that are hosting the biotin, a phosphatidycholine lipid bilayers or a fatty acid monolayer, in contrast to our surfaces which are a biotin terminated PEG oligomers grafted at relatively low density to a glass surface. Although there have been several studies of the binding of avidin pro-

teins to self assembled monolayers of biotinylated thiols on gold surfaces which more closely resemble our system (see for example Knoll et al[115,120–123], Slayton et al[124–126] and Seifert et al[127]), they have not examined quantitatively the kinetics of binding of the protein to the surface. A second reason, which may be more significant, is the fact that the studies of Reichert et al and Conboy et al did not account in their experiments for the contribution of diffusion of the protein to the biotinylated surfaces. In these studies the Langmuir kinetic equation is used ($\frac{\partial \Gamma}{\partial t} = k_a c_s \{\Gamma - \Gamma_\infty\}$), and the sublayer concentration c_s is assumed to be equal to the bulk concentration c_o. As a result of bulk diffusion gradients, this is not the case and the overall effect in fitting the kinetic equation to the measurements is to obtain an apparent k_a which is lower than the actual value as a result of the fact that c_s is smaller than c_o. In our study, the sublayer concentration c_s is correctly obtained by solving the convective diffusion equation and hence our value of k_a represents the actual kinetic constant and as such should be larger than the apparent value inferred when diffusion is ignored.

The kinetics of binding of the reverse system of biotin in solution to microbeads functionilized with Streptavidin has been studied by Huang et al[118] for polystyrene latex microbeads. In this study, the complexing of biotin conjugated with DNA to the latex microbeads was undertaken in solution under stirring, and the binding to a Langmuir equation (without saturation) was fit to obtain values for k_a in the range of 10^5 - 10^7 $M^{-1}sec^{-1}$, depending on the microbead size and number of DNA base pairs linked to the biotin. The mass transfer study of Bau et al[71] examined the kinetics of binding of biotin (fluorescently labelled with a quantum dot) in solution to Streptavidin agrose beads arrayed in a microfluidic cell, and found a value of 1.65×10^5 M^{-1} sec^{-1} using a Langmuir formulation for the kinetic binding in which the fraction of sites available for binding was corrected to account for the covering of the biotin-QD complex to unbound surface protein. The Bau et al study accounted for convection and diffusion around the microbeads, which were sandwiched between the top and bottom surfaces of the cell and as such their k_a is an intrinsic kinetic constant. Their value is larger than ours, and may be due to the fact that our study does not account specifically for the reduction in the kinetic rate due to the fact that the binding of the protein overlaps unbound biotin. Thus our value of k_a inferred by matching with the experiments is lower than the intrinsic value due to this effect, and explains the reason our value is smaller than the Bau et al[71] value.

As noted in the discussion of the transport simulations, diffusion limitations on the binding of target to the surface probes on the completely recessed microbeads arises because only the top part of the microbead surface contacts the flow, and the comparison of theory and experiment in Fig. 8 confirms this limitation. Elevating the microbeads by decreasing the depth

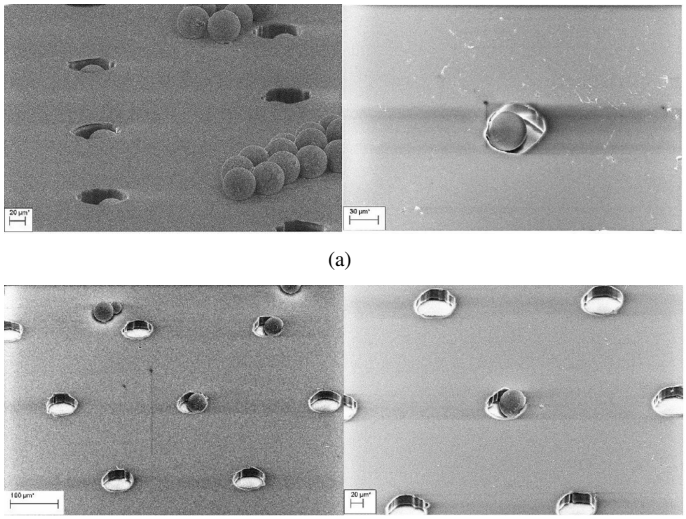

(a)

(b)

Fig. 9 SEM images of the bottom surface of a microfluidic channel: (a) for a well depth of 50μm in which the microbeads are recessed and (b) for a well depth of 25μm, showing that part of the micro bead surface is above the well plate and can intersect the flow.

of the wells has the advantage of allowing a greater area of the microbead surface to intersect the flow and transport target through a thin diffusion boundary layer (Fig. 10(a)). To examine this idea, experiments were undertaken on a recessed geometry in which only the well depth d was changed, with d reduced from 50 μm to 25 μm. Otherwise the flow rate and concentration of labelled NeutrAvidin were the same as in the experiments with the completely recessed microbeads of Fig. 8. To provide a visual picture of the microbeads in the partially recessed wells, scanning electron microscope (SEM) images of the microbeads in the microwells were obtained and compared with the configuration in which the microbeads are completely recessed. Images were recorded using a field emission SEM (Zeiss Supra55VP), and are shown in Fig. 9. The images were taken by first placing the unfunctionalized glass microbeads directly on the PDMS well plate which comprised the bottom half of the microfluidic cell, and allowing the microbeads to fall into the wells. The plate was left uncovered, and placed in the vacuum chamber of the SEM. The PDMS well plate is an insulating sample which builds up surface charge at high vacuum; the images in Fig. 9 were recorded in a variable pressure mode which introduces ionizable gas to reduce the charge buildup. The images show clearly that the partially recessed microbeads expose a greater surface area for intersection with the channel flow.

The experimental results for the normalized binding curve as a function of nondimensional time are given in Fig. 10(b) for the partially recessed microbeads, and by comparison with the binding curve of Fig. 8 for completely recessed mi-

crobeads, it is clear that the transport rate has increased. The experiments on the partially recessed microbeads were simulated for Pe = 5600 and $\varepsilon = .015$, which are the conditions of the completely recessed experiments, and a value for Da = 3.5, which was obtained by the fitting of the experimental binding curve for the completely recessed microbeads. The numerical simulations are shown in Fig. 10(b), alongside the ideal kinetic limit for this value of Da and ε (i.e. $\frac{\Gamma(\tau)}{\Gamma_\infty} = 1 - e^{-\varepsilon Da \tau}$). The simulations demonstrate that decreasing the well depth by half so that half of the microbead is exposed to the flow enhances the transport to the extent that the simulated binding curve (the dotted line) lies just below and is nearly indistinguishable with the kinetic limit (solid line) for these values of Da, Pe and ε, while for the completely recessed microbeads, the simulated binding curve for these parameters (the dotted line of Fig. 8) lies much further below the identical kinetic limit (solid line in Fig. 8). The experimental data is in agreement with the simulations, and from this agreement it is is clear that the transport to the partially recessed microbeads under these conditions is kinetically limited. The fact that the transport of target to the probes on partially recessed microbeads is equivalent to the kinetic limit implies that this recessed microbead configuration is as equivalent to the transport to circular patches on the micro channel floor. For the circular patches, Fig. 6, showed that for Pe equal to 10^4 and Da=1 (conditions resembling the microbead experiments), the transport was as well kinetically limited.

Elevation of the microbeads to the flow represents a simple solution to the attenuation of the mass transfer for microbeads completely sequestered in the wells. It is important to note however, that exposing the microbeads to the flow increased the potential for the microbeads to roll out of the wells by the torque exerted on the microbeads with the flow. For the flow rate used in the experiments in Fig. 8 and 10, 100 $\mu\ell$/min, both the recessed and partially recessed microbeads remained in the wells. Additional experiments indicated that the microbeads were retained in the wells up to flow rates of 500 $\mu\ell$/min; for larger values the microbeads began to roll out of the wells.

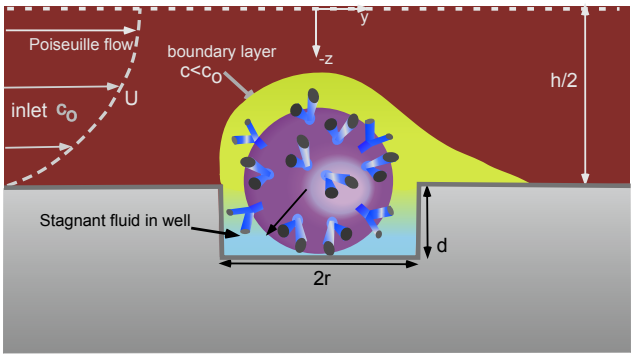

(a)

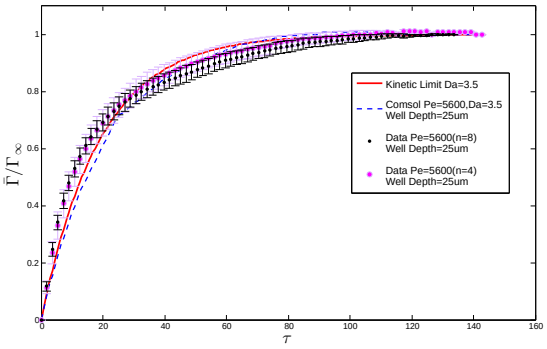

(b)

Fig. 10 (a) Partially recessed microbeads intersect more of the flow, allowing the boundary layer to cover a greater surface area of the microbead and enhance the transport rate. (b) Normalized binding curve $\bar{\Gamma}/\Gamma_\infty$ as a function of nondimensional time τ for well depth d = 25 μm, and comparison with simulation for Pe = 5600, Da = 3.5, ε = .015 for c_o = 4.2×10^{-9}M.

Conclusions

This paper has examined a prototype microfluidic platform for the screening of the binding interactions of a target biomolecule (under particular consideration a protein) against a library of probe biomolecules which represent potential binding partners. The probe molecules are hosted on the surface of glass microbeads, each displaying a separate probe, and the library is constructed by arraying the microbeads in recessed circular wells arranged at the bottom of a wide channel of a microfluidic cell. The microbeads are assembled in the wells by streaming a microbead suspension through the channel, and allowing the microbeads to settle by gravity into the wells where they are individually captured. The target analyte is flowed through the cell, and binds to the surface probes that are their binding partners; by fluorescently labeling the target, and examining the bead library for fluorescing beads, binding events are recognized and the target is screened in one step against the library.

The focus of the study has been on the mass transfer of the target to the microbead surface, a process which involves diffusion from the convective flow over the beads, followed by kinetic binding to the surface probes. Finite element numerical solutions were first developed for the low Reynolds number analyte flow over the microbeads. The streamline patterns demonstrated that fluid streams over the top part of the mi-

crobead surface, while the fluid in the well interior surrounding the bottom part of the microbead remains relatively stagnant, revolving in a very slow vortex driven by the channel shear flow over the well. Finite element calculations of the target mass transfer simulated the surface concentration of target on the bead surface as a function of time in nondimensional form as a function of the ratio of the convective to diffusive target transport rate (Peclet number, Pe), and the ratio of the kinetic rate of binding of the target to the surface probes (modelled using a Langmuir scheme) to the rate of diffusion to the probe surface (Damkohler number, Da). Peclet numbers in the range of 10 - 10^4 are typical and correspond to a mass transfer regime in which the target concentration remains uniform except in a boundary layer over the top of the bead surface where the analyte stream contacts the bead, and in the well interior surrounding the lower part of the bead surface which is cut-off from the mian flow. Target diffuses from the channel flow to the bead surface through the boundary layer to reach the top part of the bead, and through the stagnant liquid in the well to reach the bottom part. The time required to diffuse around the microbead is longer than through the boundary layer, and consequently the surface concentration on the lower part of the microbead lags behind the top part. We compare the average rate at which target binds to the microbead surface to the average rate at which it binds to circular patches of probes of the same diameter as the well diameter, and find for all *Pe* and *Da* the average binding rate is faster on the patches as a result of the barrier due to the stagnant fluid in the well. For fixed Pe, as Da decreases, the concentration gradients in the boundary layer and the stagnant fluid decrease and the transport approaches the ideal kinetic limit in which the bulk concentration is equal to the inlet concentration. We also undertook experiments on this prototype platform, assaying the binding of fluorescently labelled NeutrAvidin to its binding partner biotin, covalently bound as the probe to the bead surface. For a relatively high flow rate corresponding to Pe of order 10^3, the measured concentration on the bead surface as a function of time (obtained from the increase in fluorescence) was compared to the numerical simulations to measure the NeutrAvidin-biotin kinetic rate constant k_a. The comparison demonstrated that the overall binding rate was slower than the kinetic limit (which is commonly assumed in microfluidic binding assays), with barriers due principally to the concentration gradients in the stagnant liquid around the well limiting the transport.

Additional simulations and experiments were undertaken to examine how the diffusion limitation to the transport of the target to the surface probes on the microbead surface due to the stagnant layer of fluid surrounding the microbead in the well can be reduced by reducing the well depth so that the microbeads are not completely recessed. For the case in which the well depth is reduced by half so that half of the bead surface is exposed to the flow, the experiments demonstrated an enhanced transport under identical assay conditions of concentration and flow rate. Simulations of these experiments in the partially recessed geometry using the kinetic constant established from the completely recessed well experiments were in excellent agreement with the experimental results, and indicated that the transport rate was now kinetically controlled. While in these experiments, our platform displays only a single probe (biotin) and targets only one biomolecule (NeutrAvidin), the design is general enough to display other probes and screen multiple targets in a true library format.

Acknowledgements

This work was partially supported by an NSF grant to the Center for the Exploitation of Nanostructures in Sensors and Energy Systems (CENSES), an Army Research Office grant ARO W911NF-11-1-0161 and a NSF grant CBET 0829052.

References

1 E. C. Hulme, *Receptor-Ligand Interactions: A Practical Approach*, Oxford University Press, New York, 1992.
2 D. Lauffenburger and J. Linderman, *Receptors: Models for Binding, Trafficking and Signaling*, Oxford University Press, New York, 1993.
3 R. Hertzberg and A. Pope, *Current Opinion in Chemical Biology*, 2000, **4**, 445–451.
4 J. Groves, *Current Opinion in Drug Discovery and Development*, 2002, **5**, 606–612.
5 R. Kumar and D. Clark, *Current Opinion in Chemical Biology*, 2006, **10**, 162–168.
6 Y. Fang, Y. Hong, B. Webb and J. Lahiri, *MRS Bulletin*, 2006, **31**, 541–545.
7 E. Castellana and P. Cremer, *Surface Science Reports*, 2006, **61**, 429–444.
8 A. Chemburu, K. Fenton, G. Lopez and R. Zeineldin, *Molecules*, 2010, **15**, 1932–1957.
9 G. Walter, K. Bassow, D. Cahill, A. Lueking and H. Lehrach, *Current Opinion in Microbiology*, 2000, 298–302.
10 D. Cahill, *Journal of Immunological Methods*, 2001, **250**, 81–91.
11 H. Zhu and M. Snyder, *Current Opinion in Chemical Biology*, 2001, **5**, 40 – 45.
12 T. Kodadek, *Chem Biology*, 2001, **8**, 105–115.
13 D. S. Wilson and S. Nock, *Current Opinion in Chemical Biology*, 2002, **6**, 81 – 85.
14 S. Lal, R. Christopherson and C. d. Remedios, *DDT*, 2002, **7**, S143–S149.

15 H. Zhu and M. Snyder, *Current Opinion in Chemical Biology*, 2003, **7**, 55 – 63.

16 M. Schena, *Microarray Analysis*, John Wiley and Sons, Inc., 2003.

17 D. Yeo, R. Panicker, L. Tan and S. Yao, *Combinatorial Chemistry and High Throughput Screening*, 2004, **7**, 213–221.

18 P. Predki, *Current Opinion in Chemical Biology*, 2004, **8**, 8–13.

19 J. LaBaer and N. Ramachandran, *Current Opinion in Chemical Biology*, 2005, **9**, 14 – 19.

20 C. Hultschig, J. Kreutzberger, H. Seitz, Z. Konthur, K. Büssow and H. Lehrach, *Current Opinion in Chemical Biology*, 2006, **10**, 4 – 10.

21 C. LaFratta and D. Walt, *Chemical Reviews*, 2008, **108**, 614–637.

22 R. Wellhausen and H. Seitz, *Journal of Biomedicine and Biotechnology*, 2012, **2012**, 831347.

23 D. Vignali, *Journal of Immunological Methods*, 2000, **243**, 243–255.

24 J. P. Nolan and L. A. Sklar, *Trends in Biotechnology*, 2002, **20**, 9–12.

25 K. L. Kellar and M. A. Iannone, *Exp. Hematol.*, 2002, **30**, 1227–1237.

26 F. X. Zhou, J. Bonin and P. F. Predki, *Combinatorial Chemistry and High Throughput Screening*, 2004, **7**, 539–546.

27 D. Holmes, J. K. She, P. L. Roach and H. Morgan, *Lab on a CHip*, 2007, **7**, 1048–1056.

28 J. P. Nolan and F. Mandy, *Cytometry Part A*, 2006, **69A**, 318–325.

29 V. Krishhan, I. Khan and P. Luciw, *Crit. Rev. Biotechnol.*, 2009, **20**, 29–43.

30 H.-Y. Hsu, T. O. Joos and H. Koga, *Electrophoresis*, 2009, **30**, 4008–4019.

31 T. Buranda, J. Huang, P.-L. V., S. B., S. L. and L. G., *Analytical Chemistry*, 2002, **74**, 1149–1156.

32 W. Kusnezow, Y. V. Syagailo, S. Rüffer, K. Klenin, W. Sebald, J. D. Hoheisel, C. Gauer and I. Goychuk, *PROTEOMICS*, 2006, **6**, 794–803.

33 A. Lionello, J. Josserand, H. Jensen and H. H. Girault, *Lab on a Chip*, 2005, **5**, 254–260.

34 A. Szabo, L. Stolz and R. Granzow, *Current Opinion in Structural Biology*, 1995, **5**, 699 – 705.

35 J. Homola, *Chemical Reviews*, 2008, **108**, 462–493.

36 F. S. Ligler, *Analytical Chemistry*, 2009, **81**, 519–526.

37 R. L. Rich and D. G. Myszka, *Journal of Molecular Recognition*, 2011, **24**, 892–914.

38 A. Janshoff and S. Kunneke, *European Biophysics Journal*, 2000, **29**, 549–554.

39 A. Bernard, B. Michel and E. Delamarche, *Analytical Chemistry*, 2001, **73**, 8–12.

40 Y. Gao, G. Hu, F. Y. H. Lin, P. Sherman and D. Li, *Biomedical Microdevices*, 2005, **7**, 301–312.

41 J. A. Benn, J. Hu, B. J. Hogan, R. C. Fry, L. D. Samson and T. Thorsen, *Analytical Biochemistry*, 2006, **348**, 284 – 293.

42 E. Verpoorte, *Lab on a Chip*, 2003, **3**, 60N–68N.

43 C. Lim and Y. Zhang, *Biosensors and Bioelectronics*, 2007, **22**, 1197–1204.

44 S. Derveaux, B. Stubbe, K. Braeckmans, C. Roelant, K. Sato, J. Demeester and S. D. Smedt, *Analytical and Bioanalytical Chemistry*, 2008, **391**, 2453–2467.

45 D. Mark, S. Haeberle, G. Roth, F. Von Setten and R. Zengerle, *Chemical Society Reviews*, 2010, **39**, 1153–1182.

46 H. Andersson, C. Jönsson, C. Moberg and G. Stemme, *ELECTROPHORESIS*, 2001, **22**, 3876–3882.

47 H. Andersson, J. Jonsson, C. Moberg and G. Stemmen, *Talanta*, 2002, **59**, 301–308.

48 M. Nolte and A. Fery, *Langmuir*, 2004, **20**, 2995–2998.

49 V. Sivagnanam, A. Sayah, C. Vandevyver and M. A. M. Gijs, *Sensors and Actuators B: Chemical*, 2008, **132**, 361–367.

50 Y. Moser, T. Lehnert and M. A. M. Gijs, *Lab on a CHip*, 2009, **9**, 3261–3267.

51 P. Stevens and D. Kelso, *Analytical Chem.*, 2003, **75**, 1147–1154.

52 P. Stevens, C. Wang and D. Kelso, *Analytical Chem.*, 2003, **75**, 1141–1146.

53 J. Lee, O. Kim, J. Jung, K. Na, P. Ho and J. Hyun, *Colloids and Surfaces B: Biointerfaces*, 2009, **72**, 173–180.

54 A. Winkleman, B. D. Gates, L. S. McCarty and G. M. Whitesides, *Advanced Materials*, 2005, **17**, 1507–1511.

55 L. Filipponi, P. D. Sawant, F. Fulga and D. V. Nicolau, *Biosensors and Bioelectronics*, 2009, **24**, 1850–1857.

56 D. Walt, *Chemical Society Reviews*, 2010, **39**, 38–50.

57 T. E. Curey, A. Goodey, A. Tsao, J. Lavigne, Y. Sohn, J. T. McDevitt, E. V. Anslyn, D. Neikirk and J. B. Shear, *Analytical Biochemistry*, 2001, **293**, 178 – 184.

58 A. Goodey, J. J. Lavigne, S. M. Savoy, M. D. Rodriguez, T. Curey, A. Tsao, G. Simmons, J. Wright, S.-J. Yoo, Y. Sohn, E. V. Anslyn, J. B. Shear, D. P. Neikirk and J. T. McDevitt, *Journal of the American Chemical Society*, 2001, **123**, 2559–2570.

59 N. Christodoulides, M. Tran, P. N. Floriano, M. Rodriguez, A. Goodey, M. Ali, D. Neikirk and J. T. McDevitt, *Analytical Chemistry*, 2002, **74**, 3030–3036.

60 M. F. Ali, R. Kirby, A. P. Goodey, M. D. Rodriguez, A. D. Ellington, D. P. Neikirk and J. T. McDevitt, *Analytical*

Chemistry, 2003, **75**, 4732–4739.
61 R. Kirby, E. J. Cho, B. Gehrke, T. Bayer, Y. S. Park, D. P. Neikirk, J. T. McDevitt and A. D. Ellington, *Analytical Chemistry*, 2004, **76**, 4066–4075.
62 N. Christodoulides, S. Mohanty, C. S. Miller, M. C. Langub, P. N. Floriano, P. Dharshan, M. F. Ali, B. Bernard, D. Romanovicz, E. Anslyn, P. C. Fox and J. T. McDevitt, *Lab on a CHip*, 2005, **5**, 261–269.
63 S. Li, P. N. Floriano, N. Christodoulides, D. Y. Fozdar, D. Shao, M. F. Ali, P. Dharshan, S. Mohanty, D. Neikirk, J. T. McDevitt and S. Chen, *Biosensors and Bioelectronics*, 2005, **21**, 574–580.
64 Y.-S. Sohn, A. Goodey, E. V. Anslyn, J. T. McDevitt, J. B. Shear and D. P. Neikirk, *Biosensors and Bioelectronics*, 2005, **21**, 303–312.
65 J. V. Jokerst, A. Raamanathan, N. Christodoulides, P. N. Floriano, A. A. Pollard, G. W. Simmons, J. Wong, C. Gage, W. B. Furmaga, S. W. Redding and J. T. McDevitt, *Biosensors and Bioelectronics*, 2009, **24**, 3622–3629.
66 J. V. Jokerst, J. W. Jacobson, B. D. Bhagwandin, P. N. Floriano, N. Christodoulides and J. T. McDevitt, *Analytical Chemistry*, 2010, **82**, 1571–1579.
67 N. Du, J. Chou, E. Kulla, P. N. Floriano, N. Christodoulides and J. T. McDevitt, *Biosensors and Bioelectronics*, 2011, **28**, 251–256.
68 J. Chou, N. Du, T. Ou, P. Floriano, N. Christodoulides and J. McDevitt, *Biosensors and Bioelectronics*, 2012, **12**, year.
69 X. Qiu, J. Thompson, Z. Chen, C. Liu, D. Chen, S. Ramprasad, M. Mauk, S. Ongagna, C. Barber, A. Abrams, D. Malamud, P. Corstjens and H. Bau, *Biomedical Microdevices*, 2009, **11**, 1175–1186.
70 J. Thompson, X. Du, J. Grogan, M. Schrlau and H. Bau, *Journal of Micromechanics and Microengineering*, 2010, **29**, 115017.
71 J. A. Thompson and H. H. Bau, *Journal of Chromatography B*, 2010, **878**, 228 – 236.
72 C. W. Kan, A. J. Rivnak, T. G. Campbell, T. Piech, D. M. Rissin, M. Mosl, A. Peterca, H.-P. Niederberger, K. A. Minnehan, P. P. Patel, E. P. Ferrell, R. E. Meyer, L. Chang, D. H. Wilson, D. R. Fournier and D. C. Duffy, *Lab on a CHip*, 2012, **12**, 977–985.
73 W. H. Henley, P. Dennis and J. M. Ramsey, *Analytical Chemistry*, 2012, **84**, 1776–1780.
74 K. Barbee and X. Huang, *Analytical Chemistry*, 2008, **80**, 2149–2154.
75 K. D. Barbee, A. P. Hsiao, M. J. Heller and X. Huang, *Lab on a CHip*, 2009, **9**, 3268–3274.
76 K. D. Barbee, A. P. Hsiao, E. E. Roller and X. Huang, *Lab on a CHip*, 2010, **10**, 3084–3093.
77 W. Xu, K. Sur, H. Zeng, A. Feinerman, D. Kelso and J. Ketterson, *Journal of Micromechanics and Microengineering*, 2008, **18**, 075027.
78 B. Lok, Y. Cheng and C. Robertson, *Journal of Colloid and Interface Science*, 1983, **9**, 104–116.
79 R. W. Glaser, *Analytical Biochemistry*, 1993, **213**, 152–161.
80 P. Schuck and A. P. Minton, *Analytical Biochemistry*, 1996, **240**, 262–272.
81 M. Yarmush, D. Patankar and D. Yarmush, *Molecular Immunology*, 1996, **33**, 1203–1214.
82 L. L. H. Christensen, *Analytical Biochemistry*, 1997, **249**, 153–164.
83 D. Myszka, T. Morton, M. Doyle and I. Chaiken, *Biophys Chem*, 1997, **64**, 127–137.
84 D. Myszka, X. He, M. Dembo, T. Morton and B. Goldstein, *Biophysical Journal*, 1998, **75**, 583–594.
85 D. Edwards, B. Golstein and D. Cohen, *J. Math. Biol.*, 1999, **39**, 533–561.
86 D. Edwards, *IMA J. Appl. Math.*, 1999, **63**, 89–112.
87 T. Mason, A. Pineda, C. Wofsy and B. Goldstein, *Mathematical Biosciences*, 1999, **159**, 123–144.
88 B. Goldstein, D. Coombs, X. He, A. R. Pineda and C. Wofsy, *Journal of Molecular Recognition*, 1999, **12**, 293–299.
89 C. Wofsy and B. Goldstein, *Biophysical Journal*, 2002, **82**, 1743–1755.
90 A. Lionello, J. Josserand, H. Jensen and H. H. Girault, *Lab on a Chip*, 2005, **5**, 1096–1103.
91 M. Zimmermann, E. Delamarche, M. Wolf and P. Hunziker, *Biomedical Microdevices*, 2005, **7**, 99–110.
92 K. Lebedev, S. Mafe and P. Stroeve, *Journal of Colloid and Interface Science*, 2006, **296**, 527–537.
93 T. Gervais and K. Jensen, *Chemical Engineering Science*, 2006, **61**, 1102–1121.
94 G. Hu, Y. Gao and D. Li, *Biosensors and Bioelectronics*, 2007, **22**, 1403–1409.
95 T. Squires, R. Messinger and S. Mannalis, *Nature Biotechnology*, 2008, **26**, 417–426.
96 H. Parsa, C. Chin, P. Mongkolwisetwara, B. Lee, J. Wang and S. Sia, *Lab on a Chip*, 2008, **8**, 2062–2070.
97 H. Sipova, D. Vrba and J. Homola, *Analytical Chemistry*, 2011, **84**, 30–33.
98 K. Subramaniam and S. Chakraborty, *Microfluidics and Nanofluidics*, 2011, **10**, 821–829.
99 R. Hansen, H. Bruus, T. H. Callisen and O. Hassager, *Langmuir*, 2012, **28**, 7557–7563.
100 J. Thompson and H. Bau, *Microfluidics and Nanofluidics*, 2012, **12**, 625–637.

101 J. Chou, L. Li, E. Kulla, N. Christodoulides, P. Floriano and J. McDevitt, *Lab on a Chip*, 2012, **12**, 5249–5256.

102 J. Chou, A. Lennart, J. Wong, M. F. Ali, P. N. Floriano, N. Christodoulides, J. Camp and J. T. McDevitt, *Analytical Chemistry*, 2012, **84**, 2569–2575.

103 P. Schaal and J. Talbot, *J. Chem. Phys.*, 1989, **91**, 4401–4409.

104 X. Jin, J. Talbot, G. Tarjus and L. N.-H. Wang, *J. Phys. Chem.*, 1993, **97**, 4256–4258.

105 X. Jin, J. Talbot and L. N.-H. Wang, *AIChE Journal*, 1994, **40**, 1685–1696.

106 B. Senger, J. Voegel and P. Schaaf, *Colloids and Surfaces A -Physicochemical and Engineering Aspects*, 2000, **165**, 255–285.

107 W. Deen, *Analysis of Transport Phenomena*, Oxford University Press, New York, 2nd edn., 2012.

108 B. Roy, T. Das, T. K. Maiti and S. Chakraborty, *Analytica Chimica Acta*, 2011, **701**, 6 – 14.

109 H. Bruus, *Theoretical Microfluidics*, Oxford University Press, 2008.

110 P. Shankar and M. Deshpande, *Annual Review of Fluid Mechanics*, 2000, **32**, 93–136.

111 N. Green, in *Advances in Protein Chemistry*, ed. M. Anson and J. Edsell, Academic Press, 1975, pp. 85–113.

112 M. Wilchek and E. A. Bayer, *Analytical Biochemistry*, 1988, **171**, 1–32.

113 N. Green, *Methods in Enzymology*, 1990, **184**, 51–67.

114 I. Wong and C. Ho, *Microfluidics and Nanofluidics*, 2009, **7**, 291–306.

115 J. Spinke, M. Liley, F. J. Schmitt, H. J. Guder, L. Angermaier and W. Knoll, *Journal of Chemical Physics*, 1993, **99**, 7012.

116 S. Zhao and W. Reichert, *Langmuir*, 1992, **8**, 2785–2791.

117 S. Zhao, D. Walker and W. Reichert, *Langmuir*, 1993, **9**, 3166–3173.

118 S. Huang, M. Stump, R. Weiss and K. Caldwell, *Analytical Biochemistry*, 1996, **237**, 115–122.

119 T. Nguyen, K. Sly and J. Conboy, *Analytical Chemistry*, 2012, **84**, 201–208.

120 L. Haeussling, H. Ringsdorf, F. J. Schmitt and W. Knoll, *Langmuir*, 1991, **7**, 1837–1840.

121 F. Schmitt and W. Knoll, *Biophysical Journal*, 1991, **60**, 716–720.

122 A. Schmidt, J. Spinke, T. Bayerl, E. Sackman and W. Knoll, *Biohysical Journal*, 1992, **63**, 1385–1392.

123 O. Azzaroni, M. Mir and W. Knoll, *J. Phys. Chem. B*, 2007, **11**, 13499–13503.

124 V. H. Perez-Luna, M. J. O'Brien, K. A. Opperman, P. D. Hampton, G. P. Lopez, L. A. Klumb and P. S. Stayton, *Journal of the American Chemical Society*, 1999, **121**, 6469–6478.

125 L. S. Jung, K. E. Nelson, P. S. Stayton and C. T. Campbell, *Langmuir*, 2000, **16**, 9421–9432.

126 K. E. Nelson, L. Gamble, L. S. Jung, M. S. Boeckl, E. Naeemi, S. L. Golledge, T. Sasaki, D. G. Castner, C. T. Campbell and P. S. Stayton, *Langmuir*, 2001, **17**, 2807–2816.

127 M. Seifert, M. T. Rinke and H.-J. Galla, *Langmuir*, 2010, **26**, 6386–6393.